On the Benefits of Active Aerodynamics on Energy Recuperation in Hybrid and Fully Electric Vehicles

energies

MDPI

Article

On the Benefits of Active Aerodynamics on Energy Recuperation in Hybrid and Fully Electric Vehicles

Petar Georgiev [1,2], Giovanni De Filippis [2], Patrick Gruber [1] and Aldo Sorniotti [1,*]

[1] Centre for Automotive Engineering, Faculty of Engineering and Physical Sciences, University of Surrey, Surrey GU2 7XH, UK; p.georgiev@surrey.ac.uk or petar.georgiev@mclaren.com (P.G.); p.gruber@surrey.ac.uk (P.G.)
[2] McLaren Automotive Ltd., Surrey GU21 4YH, UK; giovanni.defilippis@mclaren.com
* Correspondence: a.sorniotti@surrey.ac.uk

Abstract: In track-oriented road cars with electric powertrains, the ability to recuperate energy during track driving is significantly affected by the frequent interventions of the antilock braking system (ABS), which usually severely limits the regenerative torque level because of functional safety considerations. In high-performance vehicles, when controlling an active rear wing to maximize brake regeneration, it is unclear whether it is preferable to maximize drag by positioning the wing into its stall position, to maximize downforce, or to impose an intermediate aerodynamic setup. To maximize energy recuperation during braking from high speeds, this paper presents a novel integrated open-loop strategy to control: (i) the orientation of an active rear wing; (ii) the front-to-total brake force distribution; and (iii) the blending between regenerative and friction braking. For the case study wing and vehicle setup, the results show that the optimal wing positions for maximum regeneration and maximum deceleration coincide for most of the vehicle operating envelope. In fact, the wing position that maximizes drag by causing stall brings up to 37% increased energy recuperation over a passive wing during a braking maneuver from 300 km/h to 50 km/h by preventing the ABS intervention, despite achieving higher deceleration and a 2% shorter stopping distance. Furthermore, the maximum drag position also reduces the longitudinal tire slip power losses, which, for example, results in a 0.4% recuperated energy increase when braking from 300 km/h to 50 km/h in high tire–road friction conditions at a deceleration close to the limit of the vehicle with passive aerodynamics, i.e., without ABS interventions.

Keywords: active aerodynamics; regenerative braking; anti-lock braking system (ABS); hybrid and fully electric vehicles; optimization; energy efficiency; quasi-static model

Citation: Georgiev, P.; De Filippis, G.; Gruber, P.; Sorniotti, A. On the Benefits of Active Aerodynamics on Energy Recuperation in Hybrid and Fully Electric Vehicles. *Energies* **2023**, *16*, 5843. https://doi.org/10.3390/en16155843

Academic Editor: Byoung Kuk Lee

Received: 25 June 2023
Revised: 15 July 2023
Accepted: 27 July 2023
Published: 7 August 2023

1. Introduction

The recent emission regulations on road vehicles [1] are inducing a significant increase in the proportion of high-performance cars that use hybrid electric or fully electric powertrains. Electrified powertrains have brought new design challenges, among which is the increased vehicle mass due to the battery system.

Energy recuperation in braking is a key feature of hybrid electric vehicles (HEVs) and fully electric vehicles (FEVs). Regenerative braking recovers energy that would otherwise be converted into heat by the friction brakes and thus lost, and it reduces friction brake wear. For a given battery capacity, regenerative braking enables increases in either (i) the energy deployed for traction over a distance, e.g., a racetrack lap, or (ii) the available range for a given vehicle performance level in traction. Alternatively, brake regeneration allows a reduction in battery capacity in the design phase while maintaining the same range.

With the currently available FEV technology in the automotive market, which relies on adequately sized battery systems without using complementary solutions such as fuel cells, regenerative braking is the only available way of recovering energy into the battery

while driving. This is crucial, especially in high-performance FEVs, such as the Porsche Taycan and Rimac Nevera, for which battery mass is significantly higher than that in HEVs.

In HEVs with a parallel configuration, such as the one in this study, there are three ways of harvesting energy, depending on the driver input:

- In on-throttle scenarios, the internal combustion engine (ICE) can be used as a generator when the driver demand is below the maximum available ICE torque.
- In off-throttle scenarios, the electric machine/s (EMs) can be used to increase the drag torque and provide a one-pedal drive functionality [2].
- In on-brake scenarios, the driver braking force demand is split between the EM(s) and friction brakes.

The total equivalent deceleration associated with the EMs tends to be limited to a certain value. For example, the brake blending units supplied by Robert Bosch Gmbh, namely the ESP (Electronic Stability Program) for HEVs and the Integrated Power Brake, allow up to -0.3 g of regenerative braking deceleration [3]. The limit ensures that the regenerative braking torque can always be compensated by the friction brake actuation in an FTTI (Fault Tolerant Time Interval) in case of the sudden failure of the electric powertrain system. In electro-hydraulic brake configurations, the regenerative braking limit is determined by the size and capability of the actuator that builds the pressure.

A -0.3 g limit on the equivalent regenerative braking deceleration still allows high amounts of power to be recuperated at high speed. However, when the anti-lock braking system (ABS) engages, such a safety limit is usually significantly reduced, as the hydraulic pump and master cylinder are being used more aggressively to modulate the individual brake caliper pressures. Additionally, the regenerative torque can also adversely affect the wheel slip tracking performance of the ABS [4]. The reduction in regeneration during ABS interventions also prevents the worst-case scenario in vehicles with an electric axle with one P4 (according to the classification commonly used in the automotive industry, see [5]) EM per wheel. In such a case, if one machine fails to provide the expected braking torque, an uneven torque distribution between the left and right wheels occurs, which creates a direct yaw moment unexpected by the driver. This could steer the vehicle into another lane or off-road during emergency maneuvering [6]. In vehicles with in-wheel EMs, the ABS braking force modulation can be carried out by the electric powertrains, given their good responsiveness characteristics related to the lack of half-shafts. However, to satisfy the previously mentioned safety considerations, the total magnitude of the regenerative force can still be reduced, and the friction brakes can be used to supply the bulk of the braking force, see [7,8]. ABS interventions with regenerative braking via in-wheel motors can also affect the battery lifespan due to the resulting micro-cycling of the current, which Salari et al. tried to mitigate in [9].

Since normal driving rarely involves full braking demands (braking events with a deceleration magnitude exceeding 5 m/s^2 tend to occur only in emergency situations [10]), the reduction in regeneration during ABS activations does not significantly impact energy consumption. However, when driving a sports vehicle on a track, drivers tend to brake at the limit, which means that the ABS intervenes in almost every braking event, thus significantly reducing the regeneration opportunities.

In addition to the varying safety-related limit on brake regeneration, the tire slip power losses as well as the drivetrain power losses are detrimental to the energy recovery efficiency in braking. In particular, tire slip is the main source of power loss in proximity to the limit of handling. A significant body of literature proposes minimizing such power losses in pure traction [11,12] and in combined cornering and traction/braking [13,14] through various actuations, such as torque-vectoring. During straight-line braking in purely ICE-driven vehicles, tire slip power losses can be ignored, as the kinetic energy of the vehicle is converted into heat, regardless of whether this happens through tire slip, friction between brake disks and pads, or aerodynamic drag. When regenerative braking is active, however, the longitudinal slip power losses decrease the regenerative power because of the associated decrease in wheel speed. This only occurs at speeds for which the regeneration is not power

limited by the powertrain and/or battery characteristics. Reference [15] presented an algorithm integrating the electronic braking force distribution (EBD) and the regenerative brake blending functions for a vehicle with a single EM connected to the four wheels with a 50:50 front-to-rear torque distribution. The algorithm makes the front-to-rear braking force distribution deviate from the ideal curve to ensure that the motor is regenerating at the maximum possible power whilst meeting the locking limits for the axles, which are obtained through a friction coefficient estimator. Reference [16] discussed an offline optimization for minimizing the tire–road friction utilization during braking and a rule-based algorithm for brake blending. Reference [17] dealt with offline and online versions of a torque allocation algorithm for regenerative braking on a four-wheel-drive EV, which minimizes the power losses from the electric powertrains and longitudinal tire slip.

Braking performance improvement for road vehicles has been a goal of vehicle dynamics control for more than four decades [18] through the implementation of ABS, EBD, and vehicle stability controllers to ensure the best compromise between steerability, lateral and yaw stability, deceleration [18,19], and potentially other aspects. For example, the open-loop brake force distribution algorithm in [20] reduces the pitch and heave motions by considering the different anti-dive, -lift, and -squat properties of the front and rear suspensions.

High-performance road cars have also been using active aerodynamic devices to improve deceleration capability, starting from the McLaren F1, which incorporates an active rear spoiler that raises during braking with the goal of increasing drag and rear downforce, thus counteracting the inertial and aerodynamic load transfers toward the front axle [21]. The topic of active aerodynamics for road and race cars has been widely studied. For example, reference [22] proposed a scheme to control the yaw and roll moments generated by active aerodynamic devices. A controller for the four active wings placed in the corners of a small open-wheel race car was presented in [23], which showed improved lateral acceleration capability and reduced oversteer in a step steer maneuver. An active wing was used to improve ride comfort in [24]. In [25], Ahangarnejad and Melzi implemented a control scheme that varied the angles of attack of the front and rear wings to improve stability and handling at high speeds. In [26], the same authors presented an integrated chassis control system for improving the lateral and yaw dynamics through the combination of active aerodynamics, interconnected suspensions, torque-vectoring, and active rear steering. Reference [27] dealt with a high-level supervisor for a vehicle with stability control, active suspension, and active aerodynamics, which varies the prioritization of the control modules depending on the operating conditions. In [28], the effect of an active rear spoiler was assessed in terms of braking distance and time. The effect of multiple aerodynamic setups for reducing braking distance was evaluated in [29], which examined combinations of wings and flaps installed in different locations of the body of a sports vehicle, and it showed up to a 16% reduction in braking distance from 200 km/h in high tire–road friction conditions. In [30], for a sports car with an active rear wing, Broniszewski and Piechna presented an analysis method that considers unsteady aerodynamics effects coupled with vehicle body dynamics during braking. The lap time reduction brought by active aerodynamics was examined by [31], which proposed a rule-based system that switches between three modes: (i) minimum drag; (ii) maximum drag; and (iii) balanced, which maximizes the lateral acceleration capability at each speed.

In the context of high-performance HEVs and FEVs, an important research question is to determine the aerodynamic configuration that maximizes energy recovery in braking. More downforce is usually associated with increased drag; however, this is not always the case, especially for airfoils. In fact, in multiple examples of wings, e.g., [32,33], the maximum lift or downforce is produced at the highest angle of attack before the stall point, after which the lift or downforce decreases, whereas drag significantly increases. Increasing drag is normally considered inefficient for traction and cornering; however, it can be beneficial to the vehicle deceleration envelope. For the same reason, ground effect aerodynamic devices are used when possible due to their capability to produce downforce

with less drag compared with airfoils. With an airfoil, it is not known a priori whether it is more effective for regenerative braking to maximize aerodynamic drag at the expense of the total downforce, to maximize downforce, or to operate in an intermediate condition. In fact, for a given deceleration level, there are two mechanisms through which the aerodynamics reduce the tire slip power losses: (i) increasing downforce, which increases the vertical tire load, thus reducing the magnitude of the slip ratios for the same longitudinal forces; and (ii) increasing drag, which reduces the longitudinal tire forces to achieve the target deceleration, thus reducing the slip ratios.

According to the literature review above, whilst the benefit of active aerodynamics on the deceleration capability has already been demonstrated, there is a lack of studies assessing the effect of wing control on the energy recovery during regenerative braking. Additionally, no previous publication has integrated active aerodynamics with the friction brake and electric motor torque blending with the goal of improving both deceleration capability and energy recovery.

This paper aims to fill this gap through the following contributions:

- The assessment of the effects of active aerodynamics control on the recovery efficiency of regenerative braking.
- The integration of active aerodynamics with an open-loop braking force distribution and brake blending strategy for maximizing energy recovery efficiency by reducing tire slip and drivetrain power losses.

The analysis was carried out through two optimization routines based on a quasi-static three-degree-of-freedom vehicle model. The resulting maps of the decision variables were then implemented in a time domain simulation model.

The remainder of this paper is structured as follows: Section 2 discusses the target vehicle and model formulation; Section 3 presents the optimization methodology; Sections 4 and 5 analyze the optimization and time domain results; and finally, Section 6 summarizes the main conclusions.

2. Case Study Vehicle, Model Formulations, and Workflow

2.1. Case Study Vehicle

The case study vehicle is a high-performance HEV with a P2 EM at the rear axle and two P4 EMs at the front axle, see the schematic in Figure 1. The EMs are permanent magnet synchronous motors with an axial flux layout coupled with silicon MOSFET inverters operating at a DC link voltage of 400 V. The inverters are water-cooled, while the motor stators are cooled with dielectric oil. The three EMs are identical; however, the front EMs are independently connected to the front wheels via single-speed transmissions with helical gears, unlike the rear EM, which is connected to the multiple-speed transmission of the ICE, including a differential. The focus of this study is to maximize the overall regeneration efficiency of the vehicle from wheel to battery through appropriate control without any modification of the hybrid electric powertrain components. The vehicle is equipped with a passive front wing and an active rear wing, which, according to [34], is the most common air brake setup. In fact, a front airbrake could significantly disrupt the airflow and reduce the potential downforce and drag generated by the rear wing, which would not receive a freestream airflow any longer [35]. The rear wing can vary its angle of attack, ϕ_r, between the conditions of (i) maximum efficiency in terms of the lift-to-drag ratio and maximum downforce ($\phi_r = -14$ deg) and (ii) maximum drag ($\phi_r = -60$ deg).

As the vehicle is a new design concept, the model parameters come from different sources. The inertial, geometric, and aerodynamic parameters of the passive vehicle body (excluding the wings), such as the mass, wheelbase, center of gravity height, and aerodynamic coefficients, refer to a prototype vehicle derived from a production high-performance passenger car, see Table 1. The body is assumed to have a constant drag coefficient equal to 0.30 and a net zero lift coefficient. In fact, the reference vehicle is equipped with an undertray and a diffuser, which neutralize the lift generated by the top surface of the body.

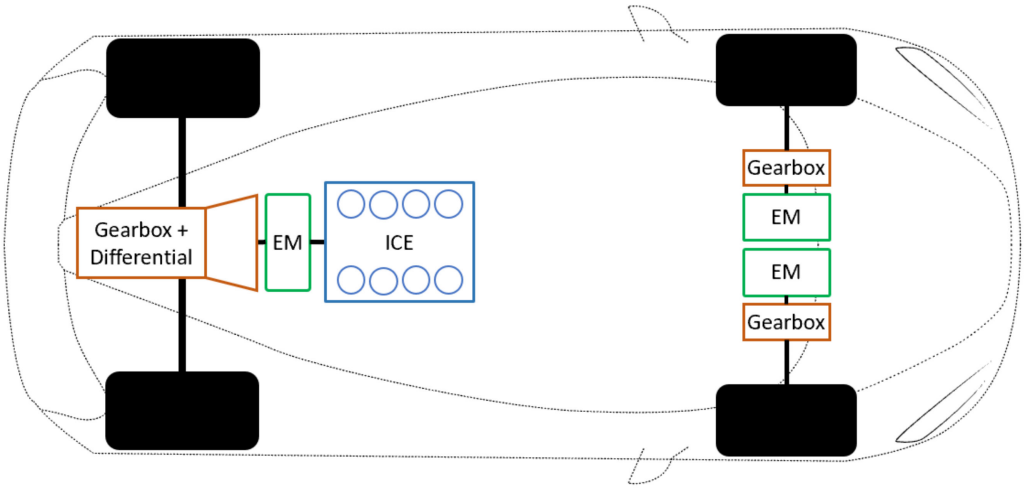

Figure 1. Schematic of the powertrain configuration of the case study HEV. The two front on-board EMs are mechanically independent, and each is connected to a gearbox; the rear motor is installed between the ICE and the rear transmission, including a gearbox and a differential.

Table 1. Main vehicle parameters.

Parameter Name	Symbol	Value
Vehicle mass	m	1650 kg
Wheelbase	l	2.69 m
Front semi-wheelbase	l_f	1.48 m
Front track width	t_f	1.68 m
Rear track width	t_r	1.61 m
Unloaded front wheel radius	$R_{w,u,f}$	0.343 m
Unloaded rear wheel radius	$R_{w,u,r}$	0.364 m
Centre of gravity height	h_g	0.44 m
Peak power of each EM	$P_{m,max}$	77 kW
Peak motoring torque of each EM	$T_{m,i,max}$	300 Nm
Peak regenerative torque of each EM	$T_{m,i,min}$	−300 Nm

The lift and drag coefficients of the two wings are based on experimental data for the NACA0012 airfoil profile [36] for a 5×10^6 Reynolds number. The vehicle is considered to consist of three independent aerodynamic devices that do not interact with each other, i.e., the body lift and drag do not change with the varying angle of attack of the wings, nor do the wings interact with each other. Despite its underlying approximation, the approach is deemed sufficiently accurate for the proof-of-concept design of an active aerodynamics controller to increase brake regeneration.

The original lift and drag coefficients of the considered airfoil are scaled to create the front and rear wings for the specific sports car, providing a total maximum 4000 N downforce at 250 km/h for the front and rear angles of attack, corresponding to the maximum efficiency of the wings, i.e., $\phi_f = \phi_r = -14$ deg, a condition that is maintained as fixed for the front one. For the same angles, the scaled wing coefficients and wing installation along the vehicle wheelbase and the vertical direction result in a downforce bias toward the rear axle by 5.3% with respect to (w.r.t.) the static weight distribution of the vehicle. Such a bias prevents the vehicle from oversteering with increasing speed. The resulting lift and drag coefficients of the rear wing, $C_{z,w,r}$ and $C_{x,w,r}$, are reported in Figure 2, which shows similar trends to those in [23].

The tire model parametrization was experimentally validated through vehicle tests and comparisons with the simulation results of an experimentally validated proprietary high-fidelity model by McLaren Automotive, e.g., in terms of the deceleration envelope. The high-fidelity model has over 14 degrees of freedom (six degrees of freedom of the

sprung mass, four degrees of freedom for the vertical motions of the unsprung masses, and four degrees of freedom associated with wheel rotations, on top of additional degrees of freedom for the steering system dynamics and compliance), considers tire nonlinearities and relaxation dynamics, and is cross-validated against established commercial tools for multi-body simulation. The efficiency maps of the front electric powertrains were obtained through experimental tests of the front electric axle on the drivetrain test rig of the University of Surrey [37], whose layout is shown in Figure 3, through which the steady-state transmission torque losses (referred to the motor speed) and the combined electric power losses of the EM and inverter were recorded for a range of speeds and torque demands, see Figure 4. The transmission torque loss reflects the efficiency from the motor output shaft to the gearbox output shaft, and the electric powertrain power loss map reflects the efficiency from the DC link of the inverter to the output shaft of the motor. The rear transmission torque loss was obtained through external experimental testing. All measurements were taken for the nominal operating temperatures of the components.

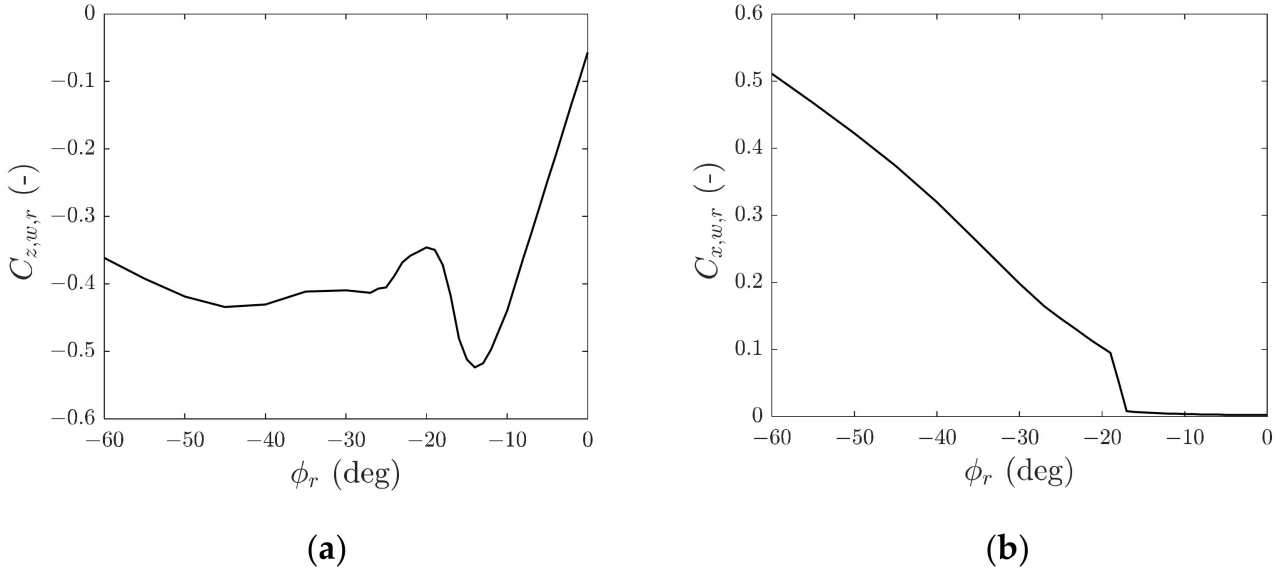

Figure 2. (**a**) Lift and (**b**) drag coefficients, $C_{z,w,r}$ and $C_{x,w,r}$, of the rear wing as a function of the angle of attack, ϕ_r.

Two aerodynamic setups of the same vehicle are considered in the remainder of this paper:

- The proposed active configuration, referred to as Active, with the variable ϕ_r.
- The Passive configuration, which serves as a baseline, in which the rear wing is held at -14 deg. This would be the setting for a vehicle with passive aerodynamic devices because it provides a good trade-off across the operating envelope. The ABS, EBD, and brake blending algorithms are the same as those for Active.

2.2. Vehicle Model Formulation

The adopted longitudinal vehicle dynamics model has 3 DoFs (degrees of freedom), which account for the longitudinal motion of the vehicle body and the rotation of the wheels and associated components of the front and rear axles, see Figure 5. In this section and the remaining sections, the notation '[ ]' indicates a factor of a product, while the notation '[ ]' indicates the independent variable of a function.

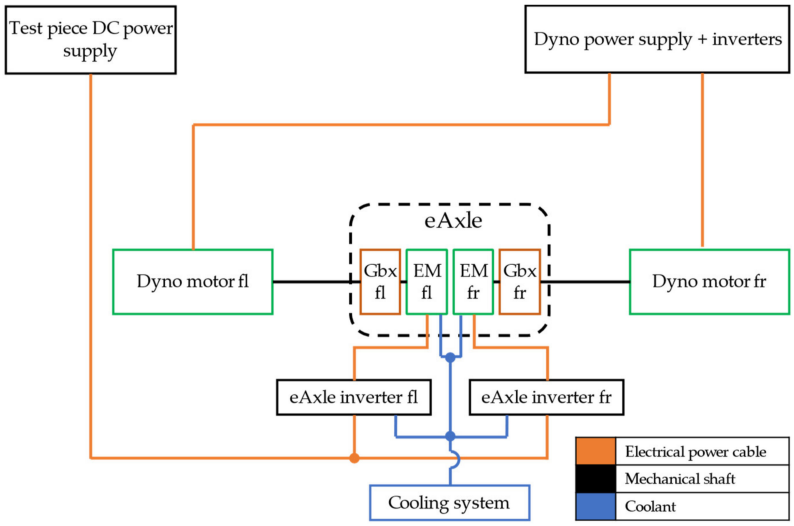

(**a**)

(**b**)

Figure 3. (**a**) Schematic of the test rig setup at the University of Surrey, including electric machines emulating the road load (Dyno motors); power supplies for the test piece and test rig inverters; inverters of the electric axle (eAxle); eAxle components, namely gearboxes (Gbx) and EMs, where the notations 'fl' and 'fr' refer to the front left and front right powertrains; and (**b**) test rig with test piece installation.

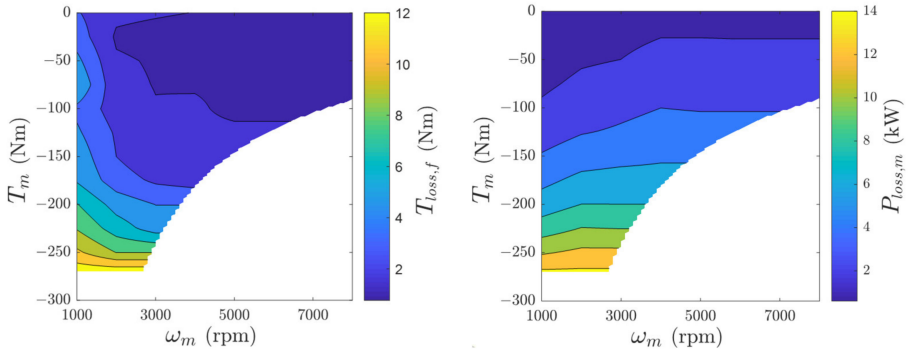

(**a**) (**b**)

Figure 4. (**a**) Torque loss ($T_{loss,f}$) map of each front gearbox, referred to at the EM shaft level, as a function of EM torque (T_m) and speed (ω_m); and (**b**) power loss map ($P_{loss,m}$) of the individual inverter and EM.

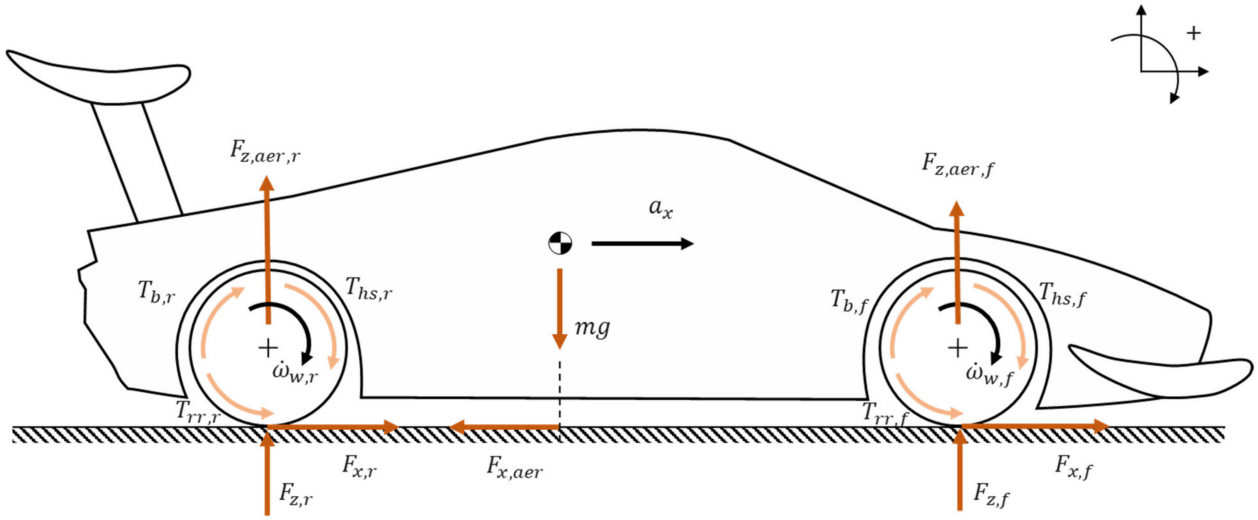

Figure 5. Schematic of the 3-DoF vehicle model with indications of the main variables and their sign conventions. The black arrows refer to accelerations, the red arrows refer to forces, and the orange arrows refer to moments.

The longitudinal force balance is:

$$ma_x = 2F_{x,f} + 2F_{x,r} - F_{x,aer} \tag{1}$$

where m is the vehicle mass; a_x is the longitudinal acceleration; $F_{x,f}$ and $F_{x,r}$ are the front and rear longitudinal tire forces; and $F_{x,aer}$ is the aerodynamic drag force. The moment balance equations for the front and rear axles are:

$$J_{y,eq,f}\dot{\omega}_{w,f} = 2T_{hs,f} + 2T_{b,f} - 2T_{rr,f} - 2F_{x,f}R_{w,l,f} \tag{2}$$

$$J_{y,eq,r}\dot{\omega}_{w,r} = 2T_{hs,r} + 2T_{b,r} - 2T_{rr,r} - 2F_{x,r}R_{w,l,r} \tag{3}$$

where $J_{y,eq,i}$ is the equivalent mass moment inertia of the rotating parts of the i-th axle, with the subscript $i = f, r.$ indicating the front or rear axle; $\dot{\omega}_{w,i}$ is the angular wheel acceleration; $T_{hs,i}$ is the half-shaft torque at the CV (constant velocity) joint of the respective wheel; $T_{b,i}$ is the friction brake torque; $T_{rr,i}$ is the rolling resistance torque; and $R_{w,l,i}$ is the laden radius of the tire.

$F_{x,f}$ and $F_{x,r}$ are calculated through version 5.2 of the Pacejka magic formula [38]:

$$F_{x,i} = D_i \sin\Big(C_i \tan\Big(B_i\sigma_i - \tan^{-1}(B_i\sigma_i)\Big)\Big) + S_{vx,i} \tag{4}$$

where σ_i is the tire slip ratio; D_i, C_i, B_i, and $S_{vx,i}$ are functions of the magic formula coefficients, the friction factor μ, and the vertical tire load $F_{z,i}$, which, by neglecting the pitch, heave, and unsprung mass dynamics, is given by:

$$F_{z,f} = \frac{1}{2}\left[\frac{mgl_r}{l} - \frac{ma_x h_g}{l} - F_{z,aer,f}\right] \tag{5}$$

$$F_{z,r} = \frac{1}{2}\left[\frac{mgl_f}{l} + \frac{ma_x h_g}{l} - F_{z,aer,r}\right] \tag{6}$$

The loaded wheel radius is computed as:

$$R_{w,l,i} = q_{re0,i}R_{w,u,i} - \frac{F_{z,i}}{C_{z,stiff,i}} \tag{7}$$

where $q_{re0,i}$ is a non-dimensional coefficient; $R_{w,u,i}$ is the unladen tire radius; and $C_{z,stiff,i}$ is the vertical tire stiffness. σ_i is calculated as:

$$\sigma_i = \frac{\omega_{w,i} R_{w,e,i} - V}{V} \tag{8}$$

where V is the vehicle speed and $R_{w,e,i}$ is the effective wheel radius, defined as:

$$R_{w,e,i} = q_{re0,i} R_{w,u,i} - \frac{F_{z,Nom,i}}{C_{z,stiff,i}} \left[D_{re,i} \tan^{-1} \left(B_{re,i} \frac{F_{z,i}}{F_{z,Nom,i}} \right) + q_{re1,i} \frac{F_{z,i}}{F_{z,Nom,i}} \right] \tag{9}$$

In (9), $F_{z,Nom,i}$ is the nominal vertical tire load; $q_{re0,i}$, $q_{re1,i}$, $D_{re,i}$ and $B_{re,i}$ are calibration coefficients. The tire rolling resistance torque is:

$$T_{rr,i} = R_{w,u,i} F_{z,i} \left[f_o + f_2 V^2 \right] \tag{10}$$

where f_o and f_2 are the rolling resistance coefficients.

$T_{hs,f}$ and $T_{hs,r}$ are given by:

$$T_{hs,f} = T_{hs,ctrl,f} - T_{loss,f} \mathrm{sgn} \left(\omega_{w,f} \right) \tag{11}$$

$$T_{hs,r} = T_{hs,ctrl,r} - T_{loss,r} \mathrm{sgn} \left(\omega_{w,r} \right) \tag{12}$$

where $T_{loss,f}$ is the torque loss of each front gearbox and $T_{loss,r}$ is half of the torque loss of the rear transmission, referred to the differential output. $T_{loss,f}$ and $T_{loss,r}$ are obtained from experimentally derived nonlinear functions, $f_{g,i}$ (see Section 2.1):

$$T_{loss,f} = f_{g,f} \left(\omega_{m,f}, T_{m,f} \right) \tag{13}$$

$$T_{loss,r} = f_{g,r} \left(\omega_{m,r}, T_{m,r}, N_g \right) \tag{14}$$

where N_g is the selected gear number and $\omega_{m,i}$ is the angular motor speed:

$$\omega_{m,i} = \omega_{w,i} i_{g,i} \tag{15}$$

where $i_{g,f}$ is the front gearbox ratio; $i_{g,r}$ is the gear ratio of the rear transmission, including the final reduction ratio; and $T_{hs,ctrl,f}$ and $T_{hs,ctrl,r}$ are the controlled half-shaft torque levels:

$$T_{hs,ctrl,f} = T_{m,f} i_{g,f} \tag{16}$$

$$T_{hs,ctrl,r} = \frac{1}{2} T_{m,r} i_{g,r} \tag{17}$$

where $T_{m,f}$ is the individual front EM torque and $T_{m,r}$ is the rear EM torque. Since the P2 EM is connected to the primary shaft of the rear gearbox, its torque is split between the two rear wheels. $T_{hs,ctrl,f}$ and $T_{hs,ctrl,r}$ are control variables, and the EM torque demands are computed by rearranging (16) and (17).

The electrical power $P_{m,e,i}$ at the DC connections of the traction inverters is calculated from the experimental power loss characteristics of the powertrains (see Section 2.1):

$$P_{m,e,i} = T_{m,i} \omega_{m,i} + P_{m,loss,i} \tag{18}$$

The total electrical power output from the battery to the powertrains, $P_{m,e,tot}$, is:

$$P_{m,e,tot} = 2 P_{m,e,f} + P_{m,e,r} \tag{19}$$

At the vehicle level, the aerodynamic forces are computed as:

$$F_{z,aer,f} = \frac{1}{2}\rho S C_{z,aer,f} V^2 \tag{20}$$

$$F_{z,aer,r} = \frac{1}{2}\rho S C_{z,aer,r} V^2 \tag{21}$$

$$F_{x,aer} = \frac{1}{2}\rho S C_{x,aer} V^2 \tag{22}$$

where ρ is the air density; S is the vehicle frontal area; and $C_{z,aer,f}$, $C_{z,aer,r}$, and $C_{x,aer}$ are the respective nondimensional aerodynamic coefficients.

The individual wing and body lift and drag coefficients, namely $C_{z,w,f}$, $C_{x,w,f}$, $C_{z,w,r}$, $C_{x,w,r}$, $C_{z,b}$, and $C_{x,b}$, are converted—by using superposition of effects—into two coefficients, $C_{z,aer,f}$ and $C_{z,aer,r}$, for the equivalent lift forces on the front and rear axles and one coefficient, $C_{x,aer}$, for the equivalent vehicle drag force, applied to an imaginary point that is the projection of the center of gravity on the ground plane. The resulting coefficients are shown in Figure 6, as a function of ϕ_r, for $\phi_f = -14$ deg. Notably, the front lift coefficient is highly dependent on the rear wing angle of attack and becomes less negative as ϕ_r becomes more negative. This is a result of the positions of the wings, which are placed lengthwise outside the wheelbase, which implies that the downforce associated with each wing increases the vertical load on the respective axle and decreases the vertical load on the opposite axle. The high installation position of the rear wing also contributes to this effect, as its drag force generates a longitudinal load transfer from the front to the rear axle.

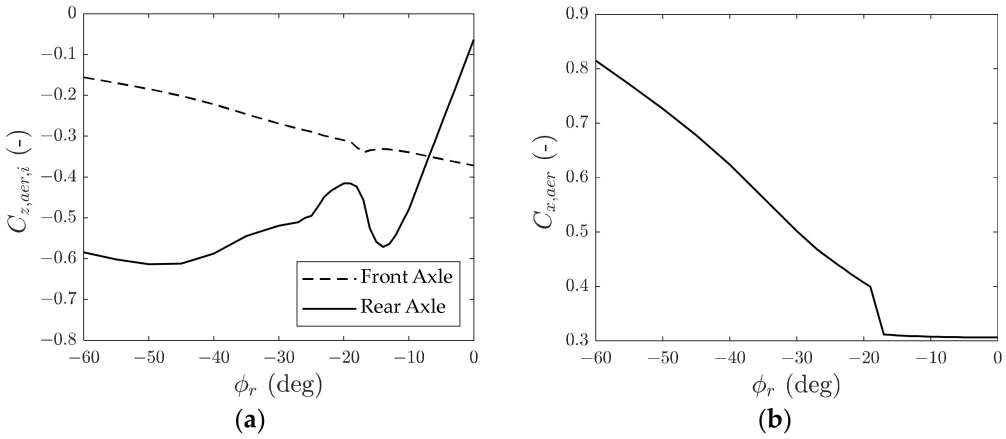

Figure 6. (**a**) Front and rear axle lift coefficients, $C_{z,aer,f}$ and $C_{z,aer,r}$, as a function of ϕ_r; and (**b**) drag coefficient at the vehicle level, $C_{x,aer}$, as a function of ϕ_r.

In the time domain implementation in Section 5, the friction brake actuation dynamics are modeled through a first-order transfer function with a time constant of 12 ms as an approximation of the experimental results from [39]. The actuation rates of the EMs and rear wing are also modeled. In particular, $|\phi_r|$ can change at up to 120 deg/s, which is equivalent to 0.5 s for the transition from 0 deg to the maximum drag mode. The rate of change of the EM torque is limited to 10^4 Nm/s.

2.3. Architecture for Time Domain Simulations

The simulation framework (see Figure 7) includes:

- The driver model, which generates the total braking force demand, $F_{x,ctrl,dem}$, which, in the real car equipped with an electro-hydraulic braking system, would be computed from the measured brake pedal position. Depending on the maneuver, the driver model is either a feedforward model demanding a given $F_{x,ctrl,dem}$ profile or a feedforward-feedback model, which adjusts the braking force demand to follow a target deceleration profile.

- The feedforward brake controller, containing lookup tables, based on the outputs of the Problem 1 and Problem 2 optimizations in Section 3, which compute (i) the actuation levels of the rear wing, ϕ_r; (ii) the controllable front and rear braking forces, $F_{x,ctrl,FF,i}$, caused by the combination of the friction braking and EM actuations; and (iii) the target front and rear half-shaft torque, $T_{hs,ctrl,FF,i}$, i.e., the regenerative braking contributions.
- The EBD, which, in case of the excessive magnitude of the rear slip ratios w.r.t. the front ones in braking, performs a reduction in the magnitude of $F_{x,ctrl,FF,r}$ and thus generates the EBD force demands $F_{x,ctrl,EBD,rj}$ according to the formulation in [19], which facilitates vehicle stability in braking. Here and in the remainder of this paper, the subscript $j = l, r$ indicates the left or right wheels, which are considered independent in the EBD regulation algorithm. Nevertheless, in the simulations, given the symmetry of the considered scenarios and the vehicle model assumptions, the response on the two vehicle sides is considered identical.
- The ABS, based on a state-of-the-art formulation for production vehicles [40], which, in the presence of wheel locking tendency on individual corners, computes an appropriate reduction ($\Delta F_{x,ctrl,ABS,ij}$) of $F_{x,ctrl,FF,F}$ and $F_{x,ctrl,EBD,rj}$, resulting in updated reference braking forces, $F_{x,ctrl,ABS,ij}$. The ABS modulation is actuated solely by the friction brakes, as the EMs are connected to the wheels by transmissions and half-shafts, which prevent sufficiently accurate torque control.
- The brake blending algorithm, which, starting from $F_{x,ctrl,ABS,ij}$, outputs the torque demands for the EMs and friction brakes, $T_{m,ij}$ and $T_{b,ij}$, respectively. The function tries to maximize the regenerative torque while accounting for (i) the EM limits; (ii) the battery power limit; (iii) the feedforward contributions $T_{hs,ctrl,FF,i}$; and (iv) the equivalent regenerative deceleration limit, $a_{x,eq,lim,saf}$, related to the functional safety considerations mentioned in Section 1, which—for conciseness—is referred to as the safety limit. While $a_{x,eq,lim,saf}$ is considered to be constant in the quasi-static optimizations of Section 3, in the more realistic time domain simulations, the magnitude of $a_{x,eq,lim,saf}$ can decrease during the ABS interventions. More specifically, in the simulations considering its variation, $a_{x,eq,lim,saf}$ ramps down from its static value of -0.3 g to -0.045 g, and then stays at this value for 1 s or until the brake blending algorithm determines that the braking system can meet the safety requirements with -0.3 g. After this time-out, the regenerative torque ramps back up to the static value within ~0.5 s. For completeness of analysis, some of the simulations in Section 5 neglect the variation of $a_{x,eq,lim,saf}$ during the ABS interventions, and therefore, they consider $a_{x,eq,lim,saf} = -0.3$ g (which corresponds to the typical nominal calibration of the algorithm; other values are also considered in the simulations).

2.4. Workflow Overview

This study follows the workflow in Figure 8 to generate the feedforward control actions in Figure 7. First, a quasi-static optimization, called Problem 1 optimization, identifies the vehicle deceleration envelope $a_{x,min}$, as well as the associated axle braking forces and rear wing angle of attack for the relevant speed range, generating a one-dimensional (1D) map of $a_{x,min}$. Secondly, another quasi-static optimization, called Problem 2 optimization, identifies the optimal actuations of the axle braking forces, $F_{x,ctrl,i}$; the regenerative control torque, $T_{hs,ctrl,i}$; and the rear wing angle of attack, ϕ_r, needed to maximize the regenerative power for the whole range of speeds and decelerations, thus producing two-dimensional (2D) maps. The parameter space for Problem 2 has the same speed range as that for Problem 1, while the range of decelerations a_x for each speed is bound by the $a_{x,min}$ values from Problem 1. The 2D maps of $F_{x,ctrl,i}$ are then post-processed to create 2D maps of the front-to-total braking force distribution ratio, b_{ft}, and the total braking force, $F_{x,ctrl,tot}$. In the time domain simulations, these maps are implemented as lookup tables for b_{ft}, $T_{hs,ctrl,i}$, and ϕ_r, where the map of $F_{x,ctrl,tot}$ is used for the set of breakpoints for the lookup tables in lieu of a_x. In fact, within a vehicle implementation, the brake pedal input corresponds to a braking force demand from the driver rather than a deceleration demand, i.e., the

demand remains the same, irrespective of the actual road gradient (the quasi-static maps are generated under the assumption of zero gradient). $F_{x,ctrl,dem}$ is split between the front and rear axles via b_{ft} to produce $F_{x,ctrl,FF,i}$. The output of the lookup table for $T_{hs,ctrl,i}$ becomes the feedforward regenerative torque, $T_{hs,ctrl,FF,i}$, and the lookup table for ϕ_r sends a demand to the rear wing.

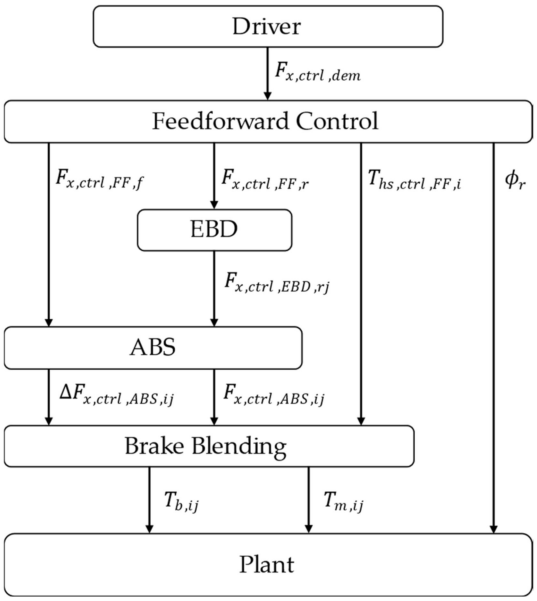

Figure 7. Simplified block diagram of the time domain simulation architecture.

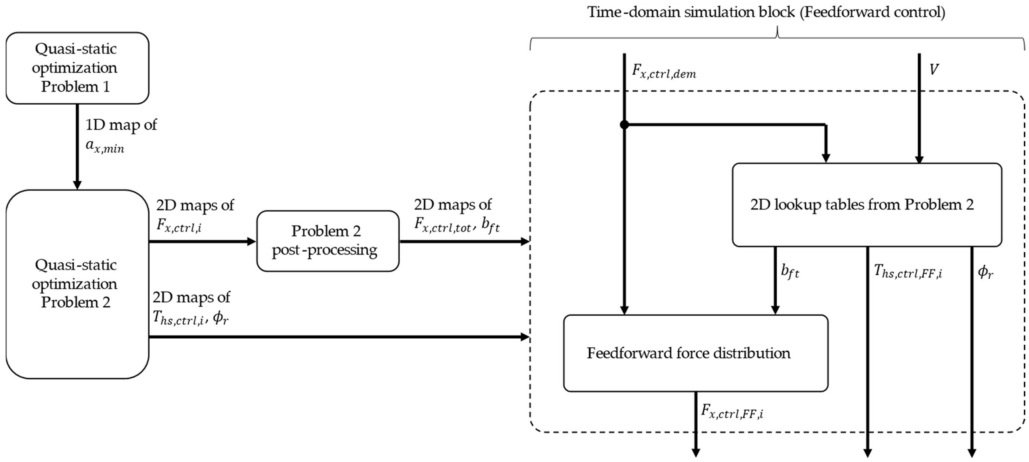

Figure 8. Workflow diagram from the quasi-static optimizations to the time domain feedforward control block.

3. Optimization Problems

The goal of the optimizations is to develop two-dimensional maps with V and a_x as entries and provide (i) the braking force on each axle; (ii) the front and rear regenerative braking contributions; and (iii) the angle of attack of the rear wing. For numerical reasons, the problem is split into two routines. Firstly, an optimization referred to as Problem 1 produces a map of the maximum deceleration as a function of V, concurrently with the corresponding braking force on each axle as well as ϕ_r, while ignoring regenerative braking. Once the so-called deceleration envelope is known, the two-dimensional actuation maps are obtained through the Problem 2 optimization, in which a_x is constrained to demanded values. Both optimization routines were implemented in MATLAB using the

'fmincon' function for constrained optimization with sequential quadratic programming as the selected numerical solver.

3.1. Problem 1

The cost function J of Problem 1 is defined as:

$$\min J(\boldsymbol{u}) = a_x \tag{23}$$

where the vector of independent variables, $\boldsymbol{u}$, is:

$$\boldsymbol{u} = \begin{bmatrix} a_x & \sigma_f & \sigma_r & F_{x,ctrl,f} & F_{x,ctrl,r} & \phi_r \end{bmatrix}^T \tag{24}$$

in which $F_{x,ctrl,i}$ is the controllable braking force at the wheel, resulting from the combination of the braking torque from the friction brakes and EM on the i-th axle. The optimization is subject to the following equality and inequality constraints:

$$ma_x = 2F_{x,f}\left(\mu, F_{z,f}, \sigma_f\right) + 2F_{x,r}(\mu, F_{z,r}, \sigma_r) - F_{x,aer}\left(V, \phi_f, \phi_r\right) \tag{25}$$

$$F_{x,ctrl,f}R_{w,l,0,f} - 2T_{rr,f}\left(F_{z,f}, V\right) - 2F_{x,f}\left(\mu, F_{z,f}, \sigma_f\right)R_{w,l,f}\left(F_{z,f}\right) = J_{y,eq,f}\dot{\omega}_{w,f}\left(\sigma_f\right) \tag{26}$$

$$F_{x,ctrl,r}R_{w,l,0,r} - 2T_{rr,r}(F_{z,r}, V) - 2F_{x,r}(\mu, F_{z,r}, \sigma_r)R_{w,l,r}(F_{z,r}) = J_{y,eq,r}\dot{\omega}_{w,r}(\sigma_r) \tag{27}$$

$$\sigma_r \geq \sigma_f - \sigma_{bias} \tag{28}$$

where $R_{w,l,0,i}$ is an averaged value of the loaded wheel radius. The equality constraints in (25)–(27) are the quasi-static versions of the dynamic equations of the system. The quasi-static approximation requires that the time derivatives of the tire slip ratios are set to zero. The inequality constraint in (28) mimics the EBD action by ensuring that the front wheels tend to lock up before the rear wheels to maintain vehicle stability in braking. This is achieved by imposing a minimum constant difference, σ_{bias}, between the front and rear slip ratios.

In the routine, $\dot{\omega}_{w,i}$ are dependent variables, which are computed from σ_i through the re-arrangement of (8), which becomes:

$$\omega_{w,i} = \frac{V[\sigma_i + 1]}{R_{w,e,i}\left(F_{z,f}\right)} \tag{29}$$

Differentiation of (29) w.r.t. time yields:

$$\dot{\omega}_{w,i} = \frac{1}{R_{w,e,i}}\left[\dot{V}[\sigma_i + 1] + \dot{\sigma}_i V\right] \tag{30}$$

which, since the quasi-static approximation implies $\dot{\sigma}_i \approx 0$, and the assumption of purely longitudinal motion implies $\dot{V} = a_x$, becomes:

$$\dot{\omega}_{w,i} = \frac{a_x[\sigma_i + 1]}{R_{w,e,i}(F_{z,i})} \tag{31}$$

3.2. Problem 2

The second optimization maximizes the regenerative power at various target deceleration levels by finding the optimal $F_{x,ctrl,i}$, $T_{hs,ctrl,i}$, and ϕ_r. The cost function formulation is:

$$\min J(\boldsymbol{u}) = -\left[P_{m,e,tot,ref} - P_{m,e,tot}\right] R_1 + \left[{\sigma_f}^2 + {\sigma_r}^2\right] R_2 + \left[\frac{P_{m,e,f}}{P_{m,e,r}} - 1\right]^2 R_3 \tag{32}$$

where R_1, R_2 and R_3 are tunable weights, and:

$$\boldsymbol{u} = \left[\begin{array}{cccccccc} a_x & \sigma_f & \sigma_r & F_{x,ctrl,f} & F_{x,ctrl,r} & \phi_r & T_{hs,ctrl,f} & T_{hs,ctrl,r} \end{array}\right]^T \tag{33}$$

The first term of J, i.e., $-\left[P_{m,e,tot,ref} - P_{m,e,tot}\right] R_1$, ensures that the regenerative power $P_{m,e,tot}$ is maximized, where $P_{m,e,tot,ref}$ is set to be 1.5% greater in magnitude than the battery power limit. This part of the cost function helps the optimization reach convergence when the battery power is greater than the current total EM power limit, since there is an incentive for all independent variables to adjust to minimize the power losses associated with tire slip, transmission, and electric powertrain components. The second and third terms of the cost function facilitate convergence when $P_{m,e,tot}$ is restricted by the maximum battery power, making the first part of J meaningless for this region of the vehicle envelope. More specifically, the second contribution of J minimizes the magnitude of the slip ratios to use the tires as efficiently as possible, which ensures the convergence of $F_{x,ctrl,f}$, $F_{x,ctrl,r}$, and ϕ_r. The third term ensures the convergence of $T_{hs,ctrl,f}$ and $T_{hs,ctrl,r}$ by targeting the even distribution of the regenerative power among the EMs.

The optimization is subject to the equality constraints in (25)–(27). A further equality constraint restricts the value of a_x to the demanded $a_{x,dem}$. This could also be achieved by making a_x an externally imposed parameter; however, this setup would make the optimization problem numerically stiff. Problem 2 is characterized by several inequality constraints, the first one being:

$$\sigma_r \geq \sigma_f - \sigma_{bias}\left(\sigma_f\right) \tag{34}$$

where σ_{bias} is proportional to σ_f, varying between 0 and the value in (28). The friction braking torques, $T_{b,f}$ and $T_{b,r}$, are defined as:

$$T_{b,i} = \frac{F_{x,ctrl,i}}{R_{w,l,0,i}} - T_{hs,ctrl,i} \tag{35}$$

and are constrained to be non-positive:

$$T_{b,i} \leq 0 \tag{36}$$

The friction brakes are assumed to be able to produce the demanded braking torque to match $F_{x,ctrl,i}$ without the assistance of the EMs. The inequality constraint in (37) emulates the regenerative torque limit imposed to meet the functional safety requirements for vehicles with regenerative braking and brake-by-wire, where $a_{x,eq,lim,saf}$ is the maximum equivalent deceleration allowed to be generated by the EMs:

$$ma_{x,eq,lim,saf} \leq \frac{T_{hs,f}}{R_{w,l,f}\left(F_{z,f}\right)} + \frac{T_{hs,r}}{R_{w,l,r}(F_{z,r})} \tag{37}$$

The torque from each motor, $T_{m,i}$, is not allowed to exceed its design envelope, which is handled through another pair of inequality constraints:

$$T_{m,i} \geq T_{m,i,min}(\omega_{m,i}) \tag{38}$$

Finally, the total electrical power from the DC connections of the inverters, $P_{m,e,tot}$, is limited according to the minimum battery power, $P_{batt,min}$, which represents the maximum charging power.

$$P_{m,e,tot} \leq P_{batt,min} \tag{39}$$

Due to the additional nonlinearities (w.r.t. the Problem 1 optimization) introduced by the torque loss models of the transmissions, the power loss models of the EMs, and the complex interaction between ϕ_r and $P_{m,e,tot}$, the Problem 2 optimization is highly non-convex with multiple local minima. To mitigate this, the optimization was run with multiple starting points for each condition in the $a_x - V$ parameter space.

4. Optimization Results

4.1. Problem 1 Results

The results of the Problem 1 optimization, which maximizes deceleration, are reported in Figure 9, which shows that Active achieves over 1 m/s^2 higher maximum deceleration than Passive. The optimal ϕ_r value for Active is -60 deg for the entire range of V. The reason can be shown through a simple point-mass vehicle model to compute the maximum deceleration for a range of ϕ_r and a fixed μ, via the following longitudinal force balance equation at the vehicle level:

$$a_{x,min} = \frac{-\mu\left[mg + F_{z,aer,f} + F_{z,aer,r}\right] - F_{x,aer}}{m} \tag{40}$$

The results from (40) are in Figure 10a, in which -60 deg is the angle of attack providing the maximum deceleration for each μ.

To generalize the analysis, Figure 10b refers to the same vehicle but with a different aerodynamic configuration using wing profiles similar to those in [25]. The profiles are scaled to produce a similar amount of total downforce to those in Figure 2, but their angles of attack are restricted to -32 deg and are not able to produce as much drag as the original wings. In this configuration, the optimal ϕ_r at $\mu = 1$ is -16 deg, corresponding to the maximum downforce position, whereas at $\mu = 0.2$, the largest deceleration is achieved by the maximum drag position, i.e., with $\phi_r = -32$ deg. Hence, interestingly, both the change in the wing profiles and tire–road friction coefficient can vary the angle of attack that maximizes deceleration. On the other hand, the change in speed does not affect the optimal ϕ_r; however, the increase in V amplifies the difference among the rear wing positions due to the increased magnitude of the aerodynamic forces.

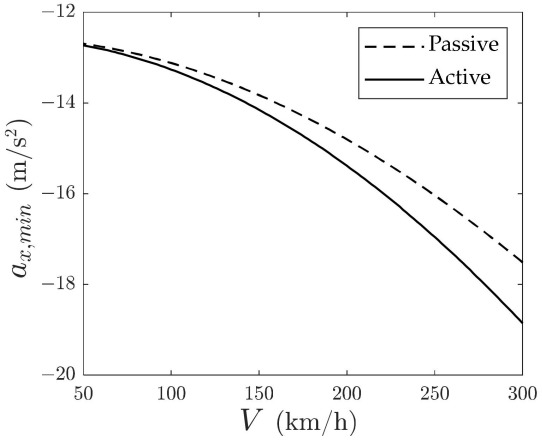

Figure 9. Results of the Problem 1 optimization: maximum deceleration, $a_{x,min}$, as a function of V for the Passive and Active configurations.

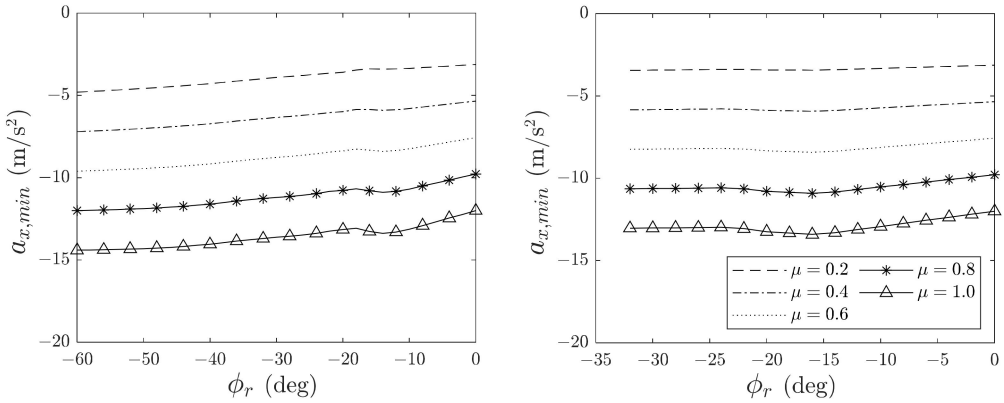

(**a**) (**b**)

Figure 10. $a_{x,min}$ as a function of ϕ_r for different values of μ, for (**a**) the airfoil used in the target vehicle of this study (see Figure 2) and (**b**) an airfoil similar to the one in [25].

4.2. Problem 2 Results

The solution of the Problem 2 optimization reveals some of the most interesting results of the study. The percentage increase in the regenerative power of Active over Passive, $\Delta P_{m,tot}$, is shown through the contour plot in Figure 11, which presents two main regions. At relatively low speeds, i.e., below ~160 km/h, the benefit of Active becomes evident as the deceleration approaches the Passive vehicle limit, with a maximum $\Delta P_{m,tot}$ value of 2.6%. The second region, above 160 km/h, which represents the critical speed, shows virtually no difference between the configurations.

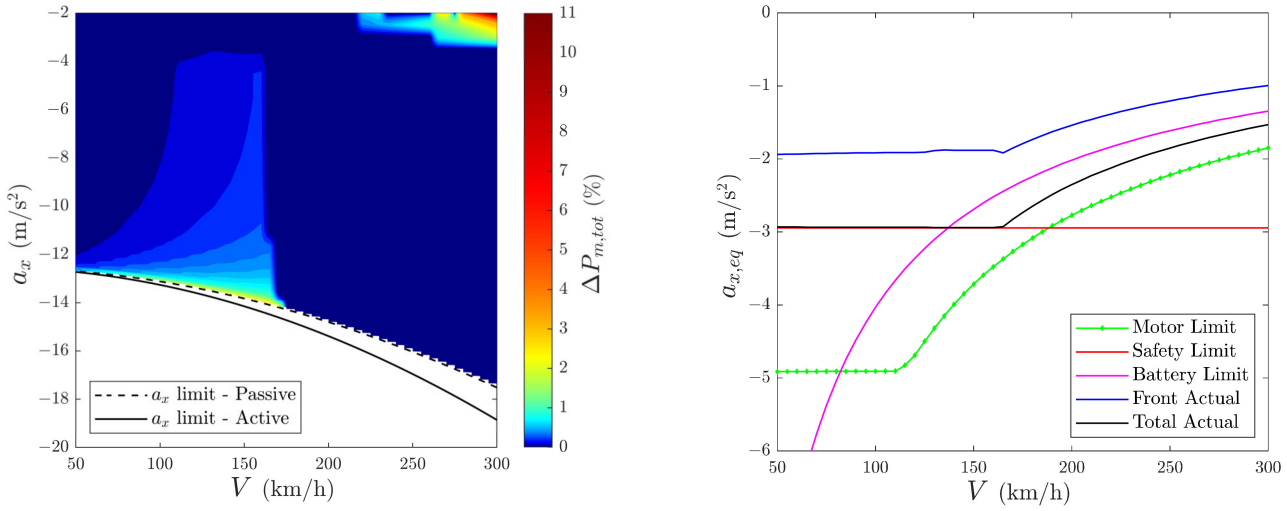

(**a**) (**b**)

Figure 11. (**a**) Contour plot of the percentage increase in regenerative power, $\Delta P_{m,tot}$, as a function of V and a_x. The dashed and continuous lines are the maximum decelerations for Passive and Active. (**b**) Equivalent decelerations—see (41)–(44)—corresponding to the EM limits ('Motor Limit'), regeneration functional safety limit ('Safety Limit'), battery limit ('Battery Limit'), actual front EM regenerative level ('Front Actual'), and actual deceleration associated with the regenerative braking effect ('Total Actual'), for $a_x = -11$ m/s^2.

The boundary dividing the two regions can be explained through Figure 11b, where the equivalent deceleration caused by regenerative braking, $a_{x,eq,m,tot}$, calculated through (41), is reported as a function of speed for $a_x = -11$ m/s^2, see the 'Total Actual' characteristic in the figure. To contextualize, the plot also includes (i) the deceleration, $a_{x,eq,lim,m}$, corresponding to the EM torque limits, see (42) and the 'Motor Limit' in the figure; (ii) the functional safety

limit, $a_{x,eq,lim,saf}$, on regeneration, equal to −0.3 g ('Safety Limit'); (iii) the deceleration, $a_{x,eq,lim,batt}$, corresponding to $P_{batt,min}$, see (43) and 'Battery Limit'; and (iv) the equivalent deceleration caused by the two front motors, $a_{x,eq,m,f}$, see (44) and 'Front Actual', which helps visualize the front-to-rear force distribution:

$$a_{x,eq,m,tot} = \frac{2\left[\frac{T_{hs,f}}{R_{w,l,0,f}} + \frac{T_{hs,r}}{R_{w,l,0,r}}\right]}{m} \tag{41}$$

$$a_{x,eq,lim,m} = \frac{2\left[\frac{T_{hs,f,min}}{R_{w,l,0,f}} + \frac{T_{hs,r,min}}{R_{w,l,0,r}}\right]}{m} \tag{42}$$

$$a_{x,eq,lim,batt} = \frac{P_{batt,min}}{mV} \tag{43}$$

$$a_{x,eq,m,f} = \frac{2\left[\frac{T_{hs,f}}{R_{w,l,0,f}}\right]}{m} \tag{44}$$

where $T_{hs,i,min}$ is the half-shaft torque computed for $T_{m,i,min}$ through (11) and (12).

The regenerative force limit is driven by $a_{x,eq,lim,saf}$ in the low-speed region and by the electrical power limit in the high-speed region. Therefore, the regenerative power benefit for the Active configuration is only present when the regenerative limit is a force limit rather than a power limit.

In the region where the regeneration is force-limited, the maximum regenerative power increases linearly with wheel speed if the transmission torque losses are ignored. Since wheel speed depends on the vehicle speed and tire slip ratio, for a given V and a_x, it is possible to increase the regenerative power by minimizing the magnitude of the slip ratios and related power losses. The regenerative benefit of active aerodynamics increases with deceleration since the slip ratio difference between Active and Passive became greater because of the nonlinearities in the tire force-slip characteristics. The increase in benefit at higher speeds is caused by the larger magnitude of the aerodynamic forces, which magnifies the difference between the two configurations.

Above the critical speed, the regenerative power is limited by the battery or the total EM power, and thus there is no difference in regenerative power between the two vehicle configurations. In Figure 11, the 'Total Actual' deceleration is not equal to the theoretical one corresponding to the battery limit because of the effect of the powertrain power losses.

The resulting maps for the optimal front-to-total brake force distribution, b_{ft}, and rear wing angle of attack, ϕ_r, are shown in Figure 12a,b. b_{ft} varies with V due to the changing vertical load balance caused by the increase in downforce and the rear bias of the downforce in the maximum drag position. ϕ_r moves to the maximum downforce position only at very low decelerations. In fact, the extra drag is only detrimental to the recuperation efficiency when the braking force demand is low enough that it can be met by the EMs alone, see the region in Figure 13 where the friction brake contribution ratio, $b_{friction}$, is approximately zero. Since $a_{x,eq,lim,saf}$ is −0.3 g, this is also approximately the threshold at which the optimization is forced to minimize drag.

At low decelerations, ϕ_r is not exactly −14 deg; on the contrary, the optimizer often found that the optimal angle of attack is approximately −17 deg. As shown in the aerodynamic maps in Figure 6, at −17 deg, the vehicle drag is only 1% higher, whereas the downforce is >10% lower. Hence, −17 deg was chosen as a trade-off between a reduction in the rolling resistance power losses by decreasing the vertical tire load and a marginal increase of the aerodynamic drag losses. For the same reason, in the top right corner of Figure 11a, $\Delta P_{m,tot}$ exceeds 10%, corresponding to 2.5 kW, since at 300 km/h, the deceleration that is caused by the aerodynamic drag and rolling resistance approaches −2 m/s^2.

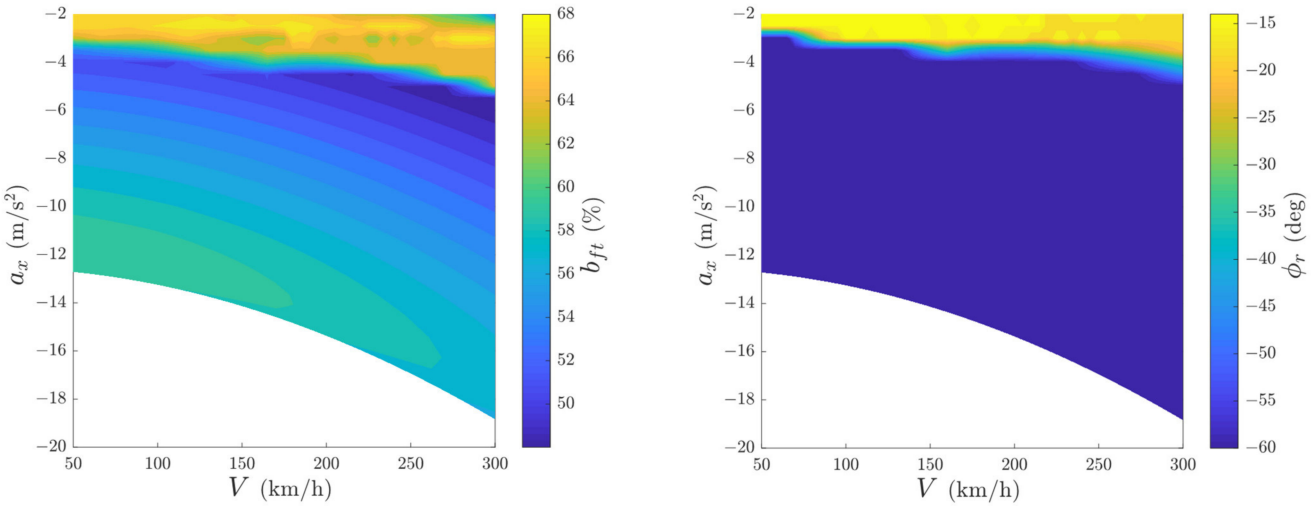

(**a**) (**b**)

Figure 12. Contour plots of (**a**) optimal front-to-total brake force distribution ratio, b_{ft} (expressed in percentage), for Active and (**b**) optimal ϕ_r for Active.

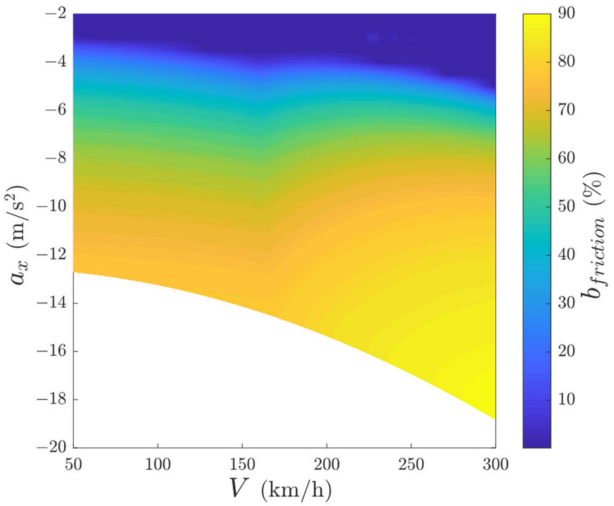

Figure 13. Contour plot of the ratio of the friction brake force to the total braking force, $b_{friction}$ (expressed in percentage), for Active.

A comparison between Active and Passive was also made for different values of $a_{x,eq,lim,saf}$. An increased magnitude of $a_{x,eq,lim,saf}$, e.g., 0.45 g, causes a decrease in the critical speed to 120 km/h, which reduces the area in which Active is beneficial. However, a lower critical speed means that the area where regeneration is limited by the battery charging power limit becomes wider, and thus the regenerated energy over a single braking event increases. Conversely, a reduced safety limit causes the critical speed and the region of benefit to increase; for example, with $a_{x,eq,lim,saf} = -0.1$ g, the critical speed exceeds 300 km/h. Interestingly, for the same vehicle speed and deceleration, e.g., 155 km/h and -13.9 m/s^2, $\Delta P_{m,tot}$ is the same, e.g., 2.5%, for $a_{x,eq,lim,saf}$ values of -0.3 g and -0.1 g. However, because for a safety limit of -0.1 g the total regenerative power for both Passive and Active is significantly lower, the increase in regenerative power brought by the controllable wing is only 1.3 kW, compared with 4.2 kW for $a_{x,eq,lim,saf} = -0.3$ g.

5. Time Domain Results

Straight-line braking tests from 300 km/h to 50 km/h were selected to compare the controllers. These maneuvers are typical of a high-performance car on a racetrack. The active and passive aerodynamic configurations were assessed for varying vehicle constraints and driver behavior. The performance metrics, reported in Table 2, are:

- The braking distance from the start of the brake pedal input application until the target speed is reached;
- The total energy recovered in the battery system during the same period;
- The peak deceleration during the maneuver.

Table 2. Performance metrics for the considered deceleration maneuvers from 300 km/h to 50 km/h. 'Max.': driver demanding the maximum deceleration level; 'Dem. < Passive': driver braking demand equal to 97% of the Passive configuration envelope; 'Passive < Dem. < Active': driver demand equal to 97% of the Passive configuration envelope plus 20% of the difference between the Active and Passive envelopes.

Test No.	Driver Deceleration Demand	Regeneration Safety Limit	Friction Correction Factor	Aerodyn. Config.	Braking Distance (m)	Total Recuperated Energy (Wh)	Peak Deceleration (m/s^2)
1	Max.	0.3 g—constant	1.00	Passive Active	235.9 227.4	205.1 197.7	16.9 17.8
2	Max.	0.3 g—variable	1.00	Passive Active	235.8 227.3	148.4 140.5	16.9 17.8
3	Dem. < Passive	0.3 g—constant	1.00	Passive Active	233.5 232.9	202.0 202.9	16.4 16.8
4	Passive < Dem. < Active	0.3 g—constant	1.00	Passive Active	233.5 228.1	206.4 199.3	16.9 17.3
5	Passive < Dem. < Active	0.3 g—variable	1.00	Passive Active	233.5 228.1	144.7 199.3	16.9 17.3
6	Dem. < Passive	0.1 g—constant	1.00	Passive Active	233.7 232.7	83.8 84.4	16.4 16.8
7	Dem. < Passive	0.5 g—constant	1.00	Passive Active	235.2 234.6	223.2 223.7	16.3 16.7
8	Dem. < Passive	0.3 g—constant	0.75	Passive Active	314.7 314.1	274.8 276.8	12.5 12.9
9	Dem. < Passive	0.3 g—constant	0.50	Passive Active	453.4 453.2	401.1 404.2	8.9 9.2

The performance trade-off for a selection of the considered tests is visualized in Figure 14, where the three axes represent the relative percentage improvement of Active over Passive in the metrics from Table 2.

Tests 1 and 2 were performed with the driver requesting the maximum deceleration, which is the usual behavior to minimize lap time. The simulations were run with constant (Test 1) and variable (Test 2) safety limits on the equivalent deceleration generated through the EMs. The braking distance and peak deceleration are approximately the same with the constant and variable $a_{x,eq,lim,saf}$. As expected, in both cases, the Active vehicle achieves 5.5% higher peak deceleration than the Passive one, along with a 3.6% shorter braking distance. Moreover, the regenerated energy is significantly lower with variable $a_{x,eq,lim,saf}$ because of the recuperation reduction during ABS actuation. In these tests, the Active configuration brings less recuperated energy than the corresponding Passive ones, by 3.6% and 5.3%. In fact, the slip ratio reaches the ABS intervention thresholds in both Active and Passive. During the ABS activation, the longitudinal tire slip power losses and regenerative power are approximately the same for a given V. However, in Active, the vehicle takes less time to achieve the same target speed due to the higher $|a_x|$, and thus the regenerated energy is lower.

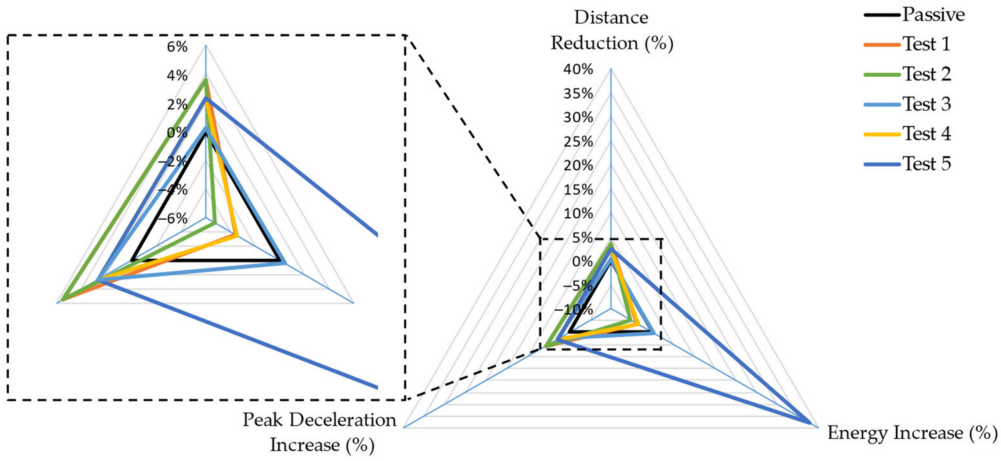

Figure 14. Spider chart showing the benefit (braking distance reduction, peak deceleration increase, and regenerated energy increase) of Active w.r.t. Passive for Tests 1–5.

To assess the energy recuperation benefit of Active in fair conditions, in Tests 3–9, the feedback driver model applies the braking force to achieve the same deceleration with Passive and Active. For example, in Test 3, the target deceleration is 97% of the envelope of Passive (see Figure 9), and therefore, the ABS is inactive. The results show that Active can brake with a 0.2% shorter distance, achieves 2.7% higher peak deceleration, and recuperates 0.4% more energy, which confirms the outputs of the quasi-static optimizations in Figure 11a.

In Tests 4 and 5, the driver demands 97% of the Passive vehicle envelope, plus 20% of the difference between the deceleration envelopes of Passive and Active, i.e., the ABS engages only for Passive. In Test 4, with constant $a_{x,eq,lim,saf}$, Active regenerates 3.5% less energy than Passive, as it takes less distance and time to reach 50 km/h. However, in the more realistic Test 5, in which $a_{x,eq,lim,saf}$ is variable, its value is subject to reduction only in Passive. This creates a significant difference in recovered energy, exceeding 37% in favor of Active, which still reduces the braking distance by 2%.

Test 5 was selected to plot the simulation time histories of Figures 15–19. The a_x and total regenerated power ($P_{regen,tot}$) profiles are in Figure 15, which highlights the extent to which the ABS activation is detrimental to regeneration at high speeds, see the time interval between ~0.7 s and ~3 s. The profiles of the total braking force contribution from the EMs and the combined regenerative and friction braking forces in Figure 16 confirm that Active needs less friction braking to achieve the same or higher decelerations, because of the additional drag applied by the active wing. Thus, the longitudinal slip ratios have a lower magnitude for Active, see Figure 17, which also shows the effect of the ABS modulation throughout the maneuver for Passive, and only between 5 s and 6 s for Active. Figure 18 reports the profiles of ϕ_r, which—for Active—goes straight to the maximum drag value and maintains it during the whole braking maneuver, according to the quasi-static optimization. For the individual front and rear wheels, indicated by the notations 'f' and 'r', Figure 19 reports (i) the EM limit; (ii) the feedforward equivalent braking force contribution from the EMs based on the quasi-static optimization maps ('FF'); and (iii) the braking force contribution limit from the EMs following the reduction caused by the ABS intervention (which varies $a_{x,eq,lim,saf}$), which is labeled as feedforward + feedback ('FF + FB'). The FB contribution is distributed between the axles in the same ratio as the feedforward force limit at the same instant.

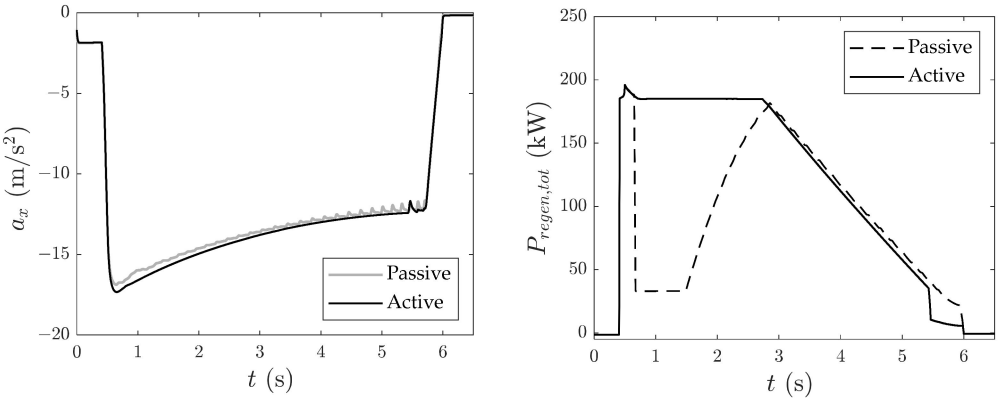

(**a**) (**b**)

Figure 15. Comparison of the Passive and Active vehicle configurations along Test 5. Time profiles of (**a**) a_x; and (**b**) total regenerative power, $P_{regen,tot}$.

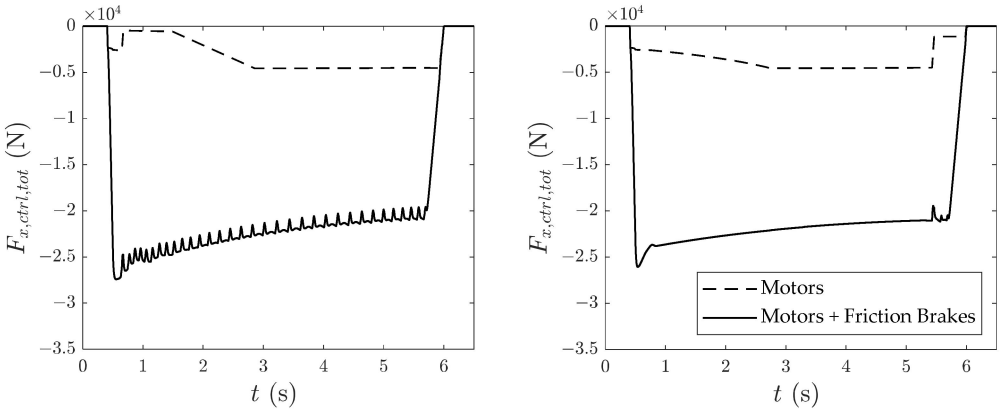

(**a**) (**b**)

Figure 16. Time profiles of the total braking force contributions, $F_{x,ctrl,tot}$, from the EMs ('Motors'), and the combination of EMs and friction brakes ('Motors + Friction Brakes'), for (**a**) Passive and (**b**) Active.

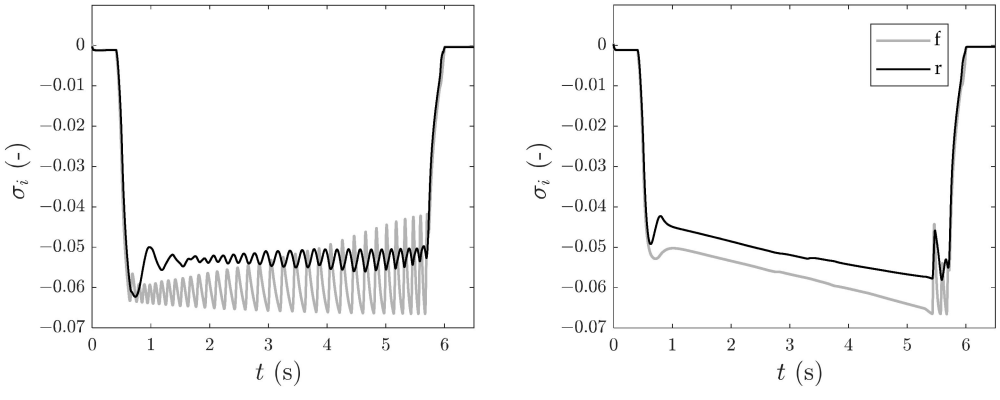

(**a**) (**b**)

Figure 17. Time profiles of the front and rear slip ratios, σ_i, for (**a**) the front ('f') and rear ('r') corners of Passive and (**b**) the front and rear corners of Active.

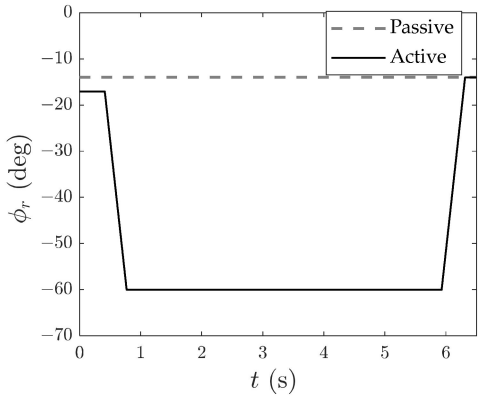

Figure 18. Time profile of ϕ_r.

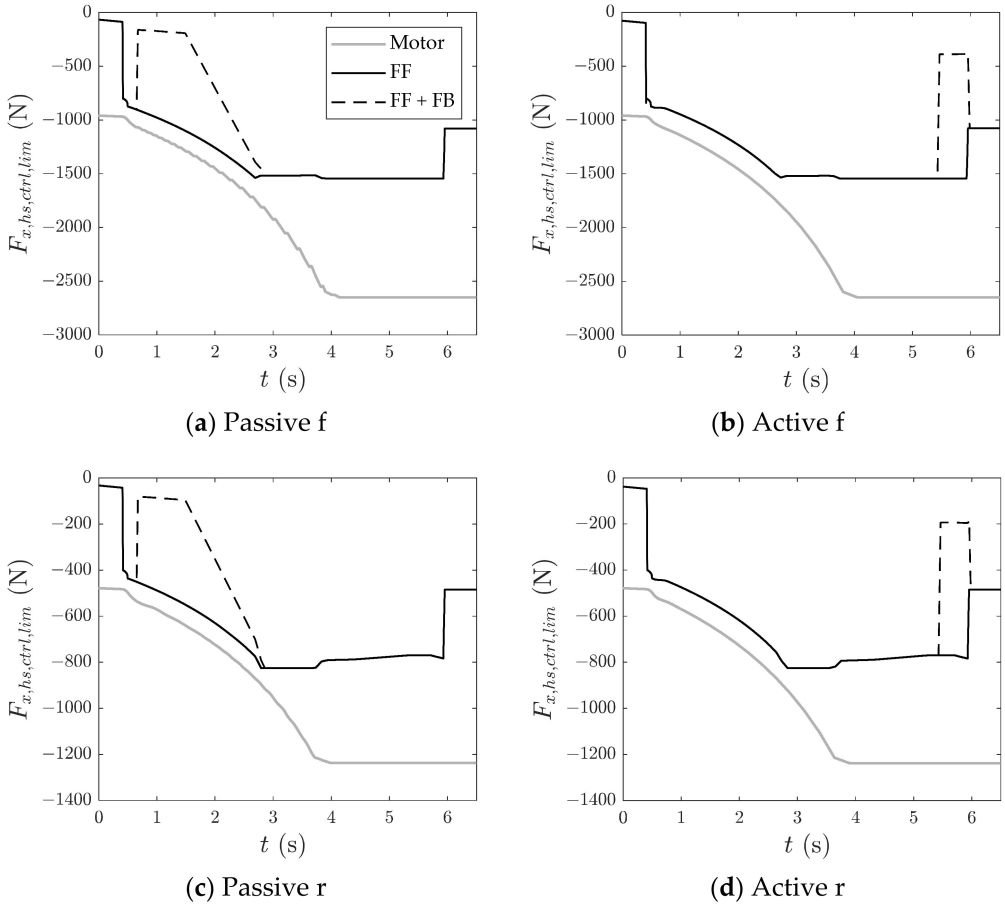

(**a**) Passive f (**b**) Active f

(**c**) Passive r (**d**) Active r

Figure 19. Time profiles of the equivalent regeneration force limits, $F_{x,hs,ctrl,lim}$, related to the EM torque characteristics ('Motor'); the feedforward ('FF') output from the map resulting from the Problem 2 optimization; and the feedforward output with the feedback correction ('FF + FB') induced by the ABS intervention with variable $a_{x,eq,lim,saf}$.

For different values of $a_{x,eq,lim,saf}$, Tests 6 and 7 in Table 2 show similar magnitudes of the recuperated energy increase in Active w.r.t. Passive. However, the relative increase is higher at lower values of $a_{x,eq,lim,saf}$, with a 0.7% increase for a safety limit of -0.1 g compared with 0.4% for -0.3 g. The reason is that the -0.1 g safety limit is the limiting factor for the entire speed range, as opposed to -0.3 g, which is only relevant for speeds below 160 km/h. For Test 7, the increase in total regenerated energy in both cases amounts to only ~10% w.r.t. Test 3. This is because the safety regeneration limit, when it is -0.5 g,

represents the limiting factor for regeneration only below 110 km/h, whereas, in the rest of the speed range, regeneration is limited by the battery and motor power.

For completeness, the analysis includes a sensitivity study with reduced tire–road friction, see Tests 8 and 9 in Table 2, which highlights that as the friction conditions (see the values of the friction correction factor) worsen, there is an increasing improvement in the regenerated energy of Active w.r.t. Passive, while maintaining the same braking distance. In comparison with the 0.4% improvement for Test 3, which is in high friction, Tests 8 and 9 show relative improvements of 0.7% and 0.8%, respectively, of Active over Passive. This is because the contribution from the aerodynamic drag is not dependent on the friction coefficient, unlike the contribution from the downforce, which is reliant on the capability of the tires to convert vertical load into longitudinal force.

6. Conclusions

This study assessed the effect of an active rear wing on energy recuperation during high-deceleration braking in a case study hybrid electric sports car. In fact, there is room for optimizing the system behavior through a non-trivial solution because of the functional safety considerations that pose a limit on the equivalent deceleration achievable through regenerative braking. Depending on the vehicle design parameters, this constraint, defined as the 'safety limit', can restrict regenerative torque more than the battery or motor power limits and can become significantly more conservative when the ABS is active.

To optimize regenerative braking performance, quasi-static optimizations were run to create maps of the optimal angle of attack and torque distribution between the axles, considering both the friction brakes and electric machines for different speeds and decelerations.

Since in the maximum downforce mode, which corresponds to the typical Passive aerodynamic setup, the rear wing is more aerodynamically efficient (i.e., it has higher downforce-to-drag ratio) than in the maximum drag mode, intuition might suggest that the maximum downforce setup also provides the highest energy recovery. However, interestingly, in both quasi-static and dynamic conditions, the results show the opposite, i.e., the maximum drag mode imposed by the Active strategy increases the regenerated energy. The reasons are as follows:

- The specific rear wing provides a higher deceleration envelope in the maximum drag mode than in the maximum downforce mode. Thus, if the safety limit decreases during ABS activation, for deceleration conditions in which the ABS is engaged only for the Passive case, the Active configuration significantly outperforms the passive one, e.g., with a regenerated energy increase by up to 37%, occurring concurrently with a 2% braking distance reduction.
- When braking at the same deceleration and from the same speed, the Active configuration reduces the longitudinal tire slip power losses because the tires have to provide less longitudinal force in comparison with the Passive case. For example, in a braking test from 300 km/h at a deceleration close to the maximum envelope of the Passive vehicle, this effect results in a 0.4% energy recovery increase, concurrently with a 0.2% braking distance reduction.

Sensitivity analyses were performed to evaluate the effect of the safety limit and tire–road friction level. The relative benefit of the Active configuration over the Passive one increases as the safety limit and tire–road friction level decrease in magnitude. For example, for the considered braking tests, a safety limit of -0.1 g implies a 0.7% increase in regenerated energy compared with 0.4% for -0.3 g, while a 0.8% improvement in regenerated energy occurs for a friction factor of 0.5 compared with 0.4% for 1.0.

The main limitations of the analysis of this research are:

- Treating the vehicle body and wings as independent aerodynamic devices that do not interact.
- The lack of consideration of the pitch dynamics in the simulations and the assumption that their influence on the aerodynamic ground effect is negligible.

- The lack of consideration of three-dimensional effects, such as vorticity and induced drag, since the considered aerodynamic coefficients are for two-dimensional airfoils.

Nevertheless, the main point of this study is that the maps of the aerodynamic coefficients as a function of the angle of attack for each active aerodynamic device are the determining factor for the respective optimal position for brake regeneration.

To facilitate the implementation of the proposed control strategy in real cars, future studies will (i) consider the energy consumption of the rear wing actuator to predict more accurately the net benefit of the system and (ii) further develop the concept of active aerodynamics with regenerative braking to include cornering conditions.

Author Contributions: Conceptualization, P.G. (Petar Georgiev) and G.D.F.; methodology, P.G. (Petar Georgiev), G.D.F., P.G. (Patrick Gruber) and A.S.; software, P.G. (Petar Georgiev) and G.D.F.; validation, P.G. (Petar Georgiev) and G.D.F.; formal analysis, P.G. (Petar Georgiev); investigation, P.G. (Petar Georgiev); data curation, P.G. (Petar Georgiev); writing—original draft preparation, P.G. (Petar Georgiev); writing—review and editing, P.G. (Patrick Gruber) and A.S.; visualization, P.G. (Petar Georgiev); supervision, G.D.F., P.G. (Patrick Gruber) and A.S.; project administration, G.D.F. and A.S.; funding acquisition, G.D.F., P.G. (Patrick Gruber) and A.S. All authors have read and agreed to the published version of the manuscript.

Funding: This research received no external funding.

Data Availability Statement: Not applicable.

Conflicts of Interest: The authors declare no conflict of interest.

Abbreviations

List of Symbols

a_x	longitudinal acceleration
$a_{x,eq,lim,batt}$	battery power related limit on the equivalent deceleration from regeneration
$a_{x,eq,lim,m}$	EM limit on the equivalent deceleration from regeneration
$a_{x,eq,lim,saf}$	safety-related limit on the equivalent deceleration from regeneration
$a_{x,eq,m,f}$	equivalent deceleration from regeneration on front axle
$a_{x,eq,m,tot}$	equivalent deceleration from regeneration on both axles
$a_{x,min}$	maximum deceleration
$b_{friction}$	ratio of the friction brake force contribution to the total braking force
b_{ft}	front-to-total braking force distribution
$C_{x,aer}$	aerodynamic drag coefficient
$C_{x,b}$	body drag coefficient
$C_{x,w,i}$	wing drag coefficient
$C_{z,aer,i}$	lift coefficient for a given axle
$C_{z,stiff,i}$	vertical tire stiffness
$C_{z,b}$	body lift coefficient
$C_{z,w,i}$	wing lift coefficient
D_i, C_i, B_i	longitudinal tire force coefficients
$D_{ref,i}$, $B_{ref,i}$, $F_{ref,i}$	effective wheel radius coefficients
f_o, f_2	tire rolling resistance coefficients
$F_{x,hs,ctrl,lim}$	limit on the controllable equivalent half-shaft force
$F_{x,i}$	longitudinal tire force
$F_{x,aer}$	aerodynamic drag force
$F_{x,ctrl,dem}$	total braking force demand
$F_{x,ctrl,i}$	axle braking force
$F_{x,ctrl,FF,i}$	axle braking force from the feedforward maps
$F_{x,ctrl,EBD,rj}$	rear wheel braking force from the EBD
$F_{x,ctrl,ABS,ij}$	wheel braking force from the ABS
$F_{z,Nom,i}$	nominal vertical tire load
$F_{z,aer,i}$	aerodynamic lift force on a given axle
$F_{z,i}$	vertical load

g	gravitational acceleration
h_g	center of gravity height
$i_{g,i}$	EM-to-wheel gear ratio
J	cost function
$J_{y,eq,i}$	equivalent mass moment of inertia of the rotating components of the axle
l	wheelbase
l_i	semi-wheelbase
m	vehicle mass
N_g	selected gear number
$P_{batt,min}$	minimum battery power, i.e., maximum battery power in regeneration
$P_{m,e,i}$	electrical power consumed or regenerated by the considered EM
$P_{m,e,tot,ref}$	reference value of the total electrical power to be consumed or regenerated by the EMs
$P_{m,e,tot}$	total electrical power consumed or regenerated by the EMs
$P_{m,loss,i}$	power loss of the considered EM
$P_{m,max}$	peak power of each EM
$P_{regen,tot}$	combined electrical power recuperation of all EMs
$q_{re0,i}$	coefficient for the computation of the loaded and effective radius
$R_{w,l,i}$	loaded wheel radius
$R_{w,l,0,i}$	averaged value of loaded wheel radius
$R_{w,u,i}$	unloaded wheel radius
R_1, R_2, R_3	cost function weights
S	frontal area of the vehicle
$S_{vx,i}$	longitudinal tire force offset
t_f, t_r	front and rear track widths
$T_{b,i}$	friction brake torque
$T_{hs,ctrl,i}$	controllable half-shaft torque
$T_{hs,i}$	half-shaft output torque
$T_{hs,i,min}$	minimum half-shaft output torque
$T_{loss,i}$	transmission torque loss
$T_{m,i}$	EM torque
$T_{m,i,max}$	maximum EM torque
$T_{m,i,min}$	minimum EM torque
$T_{rr,i}$	rolling resistance torque
$\boldsymbol{u}$	vector of optimization variables
V	vehicle speed
$\Delta F_{x,ctrl,ABS,ij}$	reduction on wheel braking force from the ABS
$\Delta P_{m,tot}$	increase in regenerative power of Active over Passive
μ	tire–road friction correction factor
ρ	air density
σ_{bias}	bound on the slip ratio difference
σ_i	longitudinal tire slip
ϕ_i	wing angle of attack
$\omega_{m,i}$	angular motor speed
$\omega_{w,i}$	angular wheel speed

List of Abbreviations

ABS	antilock braking system
EBD	electronic braking force distribution
EM	electric machine
ESP	electronic stability program
FEV	fully electric vehicle
FTTI	fault tolerant time interval
HEV	hybrid electric vehicle
ICE	internal combustion engine

References

1. *Regulation (EU) 2019/631 of the European Parliament and of the Council of 17 April 2019 Setting CO_2 Emission Performance Standards for New Passenger Cars and for New Light Commercial Vehicles, and Repealing Regulations (EC) No 443/2009 and (EU) No 510/2011*; European Union: Brussels, Belgium, 2019; Volume L 111, pp. 13–53.
2. Van Boekel, J.; Besselink, I.; Nijmeijer, H. Design and realization of a One-Pedal-Driving algorithm for the TU/e Lupo EL. *World Electr. Veh. J.* **2015**, *7*, 226–237. [CrossRef]
3. Bosch Mobility Ltd. Integrated Power Brake. Available online: https://www.bosch-mobility.com/en/solutions/driving-safety/integrated-power-brake/ (accessed on 1 June 2023).
4. Oleksowicz, S.A.; Burnham, K.J.; Barber, P.; Toth-Antal, B.; Waite, G.; Hardwick, G.; Harrington, C.; Chapman, J. Investigation of regenerative and Anti-lock Braking interaction. *Int. J. Automot. Technol.* **2013**, *14*, 641–650. [CrossRef]
5. Vacca, F.; Capilli, G.; Sorniotti, A.; Cavallino, C.; Fracchia, M.; Remondin, T.; Bottiglione, F. A novel hybridized automated manual transmission for high performance cars. In Proceedings of the 2018 IEEE 15th International Workshop on Advanced Motion Control (AMC), Tokyo, Japan, 9–11 March 2018; pp. 517–522. [CrossRef]
6. Li, L.; Li, X.; Wang, X.; Liu, Y.; Song, J.; Ran, X. Transient switching control strategy from regenerative braking to anti-lock braking with a semi-brake-by-wire system. *Veh. Syst. Dyn.* **2016**, *54*, 231–257. [CrossRef]
7. de Castro, R.; Araújo, R.E.; Tanelli, M.; Savaresi, S.M.; Freitas, D. Torque blending and wheel slip control in EVs with in-wheel motors. *Veh. Syst. Dyn.* **2012**, *50*, 71–94. [CrossRef]
8. Satzger, C.; de Castro, R.; Knoblach, A.; Brembeck, J. Design and validation of an MPC-based torque blending and wheel slip control strategy. In Proceedings of the 2016 IEEE Intelligent Vehicles Symposium (IV), Gotenburg, Sweden, 19–22 June 2016. [CrossRef]
9. Salari, A.H.; Mirzaeinejad, H.; Mahani, M.F. A new control algorithm of regenerative braking management for energy efficiency and safety enhancement of electric vehicles. *Energy Convers. Manag.* **2023**, *276*, 116564. [CrossRef]
10. Deligianni, S.P.; Quddus, M.; Morris, A.; Anvuur, A.; Reed, S. Analyzing and Modeling Drivers' Deceleration Behavior from Normal Driving. *Transp. Res. Rec. J. Transp. Res. Board* **2017**, *2663*, 134–141. [CrossRef]
11. Fujimoto, H.; Harada, S. Model-Based Range Extension Control System for Electric Vehicles With Front and Rear Driving–Braking Force Distributions. *IEEE Trans. Ind. Electron.* **2015**, *62*, 3245–3254. [CrossRef]
12. Torinsson, J.; Jonasson, M.; Yang, D.; Jacobson, B. Energy reduction by power loss minimisation through wheel torque allocation in electric vehicles: A simulation-based approach. *Veh. Syst. Dyn.* **2020**, *60*, 1488–1511. [CrossRef]
13. De Filippis, G.; Lenzo, B.; Sorniotti, A.; Gruber, P.; De Nijs, W. Energy-Efficient Torque-Vectoring Control of Electric Vehicles With Multiple Drivetrains. *IEEE Trans. Veh. Technol.* **2018**, *67*, 4702–4715. [CrossRef]
14. Kobayashi, T.; Katsuyama, E.; Sugiura, H.; Ono, E.; Yamamoto, M. Efficient direct yaw moment control: Tyre slip power loss minimisation for four-independent wheel drive vehicle. *Veh. Syst. Dyn.* **2017**, *56*, 719–733. [CrossRef]
15. Paul, D.; Velenis, E.; Cao, D.; Dobo, T. Optimal μ-Estimation-Based Regenerative Braking Strategy for an AWD HEV. *IEEE Trans. Transp. Electrif.* **2017**, *3*, 249–258. [CrossRef]
16. Biao, J.; Xiangwen, Z.; Yangxiong, W.; Wenchao, H. Regenerative Braking Control Strategy of Electric Vehicles Based on Braking Stability Requirements. *Int. J. Automot. Technol.* **2021**, *22*, 465–473. [CrossRef]
17. Sun, H.; Wang, H.; Zhao, X. Line Braking Torque Allocation Scheme for Minimal Braking Loss of Four-Wheel-Drive Electric Vehicles. *IEEE Trans. Veh. Technol.* **2018**, *68*, 180–192. [CrossRef]
18. Fling, R.; Fenton, R. A describing-function approach to antiskid design. *IEEE Trans. Veh. Technol.* **1981**, *30*, 134–144. [CrossRef]
19. Buschmann, G.; Ebner, H.-T.; Kuhn, W. Electronic Brake Force Distribution Control—A Sophisticated Addition to ABS. In *SAE Technical Paper Series*; SAE International: Warrendale, PA, USA, 1992. [CrossRef]
20. Tavernini, D.; Velenis, E.; Longo, S. Feedback brake distribution control for minimum pitch. *Veh. Syst. Dyn.* **2017**, *55*, 902–923. [CrossRef]
21. McLaren Automotive Ltd. The McLaren F1—Press Kit 1992. May 2016. Available online: https://cars.mclaren.press/en-gb/releases/375 (accessed on 1 June 2023).
22. Savkoor, A.R.; Chou, C.T. Application of Aerodynamic Actuators to Improve Vehicle Handling. *Veh. Syst. Dyn.* **1999**, *32*, 345–374. [CrossRef]
23. Diba, F.; Barari, A.; Esmailzadeh, E. Handling and safety enhancement of race cars using active aerodynamic systems. *Veh. Syst. Dyn.* **2014**, *52*, 1171–1190. [CrossRef]
24. Shahein, A.H.; Ata, A.A.; Haraz, E.H.; El-Souhily, B.M. Vibration suppression of terrains irregularities using active aero-dynamic surface for half-car model sport vehicles. *J. Vib. Control* **2020**, *26*, 2148–2162. [CrossRef]
25. Ahangarnejad, A.H.; Melzi, S. Numerical analysis of the influence of an actively controlled spoiler on the handling of a sports car. *J. Vib. Control* **2018**, *24*, 5437–5448. [CrossRef]
26. Ahangarnejad, A.H.; Melzi, S.; Ahmadian, M. Integrated Vehicle Dynamics System through Coordinating Active Aerodynamics Control, Active Rear Steering, Torque Vectoring and Hydraulically Interconnected Suspension. *Int. J. Automot. Technol.* **2019**, *20*, 903–915. [CrossRef]
27. Pinheiro, H.D.C.; Carello, M. Design and Validation of a High-Level Controller for Automotive Active Systems. *SAE Int. J. Veh. Dyn. Stab. NVH* **2022**, *7*, 83–98. [CrossRef]
28. Haggag, S.; Marzbali, M. Longitudinal Dynamics of a Vehicle Equipped with an Active Rear Spoiler. *SAE Int. J. Passeng. Veh. Syst.* **2022**, *15*, 183–194. [CrossRef]

29. Kurec, K.; Remer, M.; Piechna, J. The influence of different aerodynamic setups on enhancing a sports car\textquotesingles braking. *Int. J. Mech. Sci.* **2019**, *164*, 105140. [CrossRef]
30. Broniszewski, J.; Piechna, J. A fully coupled analysis of unsteady aerodynamics impact on vehicle dynamics during braking. *Eng. Appl. Comput. Fluid Mech.* **2019**, *13*, 623–641. [CrossRef]
31. Ferraris, A.; De Cupis, D.; Pinheiro, H.D.C.; Messana, A.; Sisca, L.; Airale, A.G.; Carello, M. Integrated Design and Control of Active Aerodynamic Features for High Performance Electric Vehicles. In *SAE Technical Paper Series*; SAE International: Warrendale, PA, USA, 2021. [CrossRef]
32. Broeren, A.; Bragg, M. Effect of Airfoil Geometry on Performance with Simulated Intercycle Ice Accretions. *J. Aircr.* **2005**, *42*, 121–130. [CrossRef]
33. Katz, J.J. Race-Car Aerodynamics. In *AccessScience*; McGraw Hill: Chicago, IL, USA, 2015. [CrossRef]
34. Piechna, J. A Review of Active Aerodynamic Systems for Road Vehicles. *Energies* **2021**, *14*, 7887. [CrossRef]
35. Devanuri, J.K. Numerical Investigation of Aerodynamic Braking for a Ground Vehicle. *J. Inst. Eng. Ser. C* **2017**, *99*, 329–337. [CrossRef]
36. Sheldahl, E.R.; Klimas, P.C. *Aerodynamic Characteristics of Seven Symmetrical Airfoil Sections through 180-Degree Angle of Attack for Use in Aerodynamic Analysis of Vertical Axis Wind Turbines*; U.S. Department of Energy Office of Scientific and Technical Information: Oak Ridge, TN, USA, 1981. [CrossRef]
37. Vacca, F.; De Pinto, S.; Karci, A.E.H.; Gruber, P.; Viotto, F.; Cavallino, C.; Rossi, J.; Sorniotti, A. On the Energy Efficiency of Dual Clutch Transmissions and Automated Manual Transmissions. *Energies* **2017**, *10*, 1562. [CrossRef]
38. Pacejka, H. *Tire and Vehicle Dynamics*, 3rd ed.; Elsevier: Oxford, UK, 2012.
39. Tavernini, D.; Vacca, F.; Metzler, M.; Savitski, D.; Ivanov, V.; Gruber, P.; Hartavi, A.E.; Dhaens, M.; Sorniotti, A. An Explicit Nonlinear Model Predictive ABS Controller for Electro-Hydraulic Braking Systems. *IEEE Trans. Ind. Electron.* **2019**, *67*, 3990–4001. [CrossRef]
40. Vignati, M.; Sabbioni, E. Force-based braking control algorithm for vehicles with electric motors. *Veh. Syst. Dyn.* **2019**, *58*, 1348–1366. [CrossRef]